ORIGINAL ARTICLE

Hall effect on MHD Jeffrey fluid flow with Cattaneo–Christov heat flux model: an application of stochastic neural computing

Muhammad Awais[1] · Huma Rehman[1] · Muhammad Asif Zahoor Raja[2] · Saeed Ehsan Awan[3] · Aamir Ali[1] · Muhammad Shoaib[1] · Muhammad Yousaf Malik[4]

Abstract

Exploration and exploitation of intelligent computing infrastructures are becoming of great interest for the research community to investigate different fields of science and engineering offering new improved versions of problem-solving soft computing-based methodologies. The current investigation presents a novel artificial neural network-based solution methodology for the presented problem addressing the properties of Hall current on magneto hydrodynamics (MHD) flow with Jeffery fluid towards a nonlinear stretchable sheet with thickness variation. Generalized heat flux characteristics employing Cattaneo–Christov heat flux model (CCHFM) along with modified Ohms law have been studied. The modelled PDEs are reduced into a dimensionless set of ODEs by introducing appropriate transformations. The temperature and velocity profiles of the fluid are examined numerically with the help of the Adam Bashforth method for different values of physical parameters to study the Hall current with Jeffrey fluid and CCHFM. The examination of the nonlinear input–output with neural network for numerical results is also conducted for the obtained dataset of the system by using Levenberg Marquardt backpropagated networks. The value of Skin friction coefficient, Reynold number, Deborah number, Nusselt number, local wall friction factors and local heat flux are calculated and interpreted for different parameters to have better insight into flow dynamics. The precision level is examined exhaustively by mean square error, error histograms, training states information, regression and fitting plots. Moreover, the performance of the designed solver is certified by mean square error-based learning curves, regression metrics and error histogram analysis. Several significant results for Deborah number, Hall parameters and magnetic field parameters have been presented in graphical and tabular form.

Keywords Cattaneo–Christov heat flux · Artificial neural network · MHD flow · Jeffery fluid · Hall current · Heat transfer · Variable thickness · Stretching sheet

List of symbols

x, y, z	Cartesian coordinate system
D_B	Brownian diffusion coefficient
a, b, c, m	Positive constants

✉ Muhammad Asif Zahoor Raja
rajamaz@yuntech.edu.tw

Muhammad Awais
awais@ciit-attock.edu.pk

Huma Rehman
humarehman173@gmail.com

Saeed Ehsan Awan
saeed.ehsan@cuiatk.edu.pk

Aamir Ali
aamir_ali@cuitatk.edu.pk

Muhammad Shoaib
dr.shoaib@cuitatk.edu.pk

Muhammad Yousaf Malik
drmymalik@hotmail.com

1   Department of Mathematics, COMSATS University Islamabad, Attock Campus, Attock 43600, Pakistan

2   Future Technology Research Center, National Yunlin University of Science and Technology, 123 University Road, Section 3, Douliou 64002, Yunlin, Taiwan, ROC

3   Department of Electrical and Computer Engineering, COMSATS University Islamabad, Attock Campus, Attock 43600, Pakistan

4   Department of Mathematics, College of Sciences, King Khalid University, Abha 61413, Saudi Arabia

T	Temperature of fluid
ν	Kinematic viscosity
B_0	Magnetic field strength
MHD	Magnetohydrodynamics
CCHFM	Cattaneo–Christov heat flux model
ANN	Artificial Neural Network
P	Pressure
S	Stress tensor
λ_1	Ratio of relaxation to the retardation times
ρ	Density
U_0	Reference velocity
n	Velocity exponent
J	Current density
p_e	Electronic pressure parameter
ρ	Density
c_p	Specific heat
κ	Thermal conductivity
α	Thermal diffusivity parameter
T_∞	Ambient temperature
γ	Thermal relaxation parameter
m	Hall parameter
θ	Dimensionless temperature
τ_{w_z}	Shear stress perpendicular to horizontal direction
Re_x	Local Reynold number
q_w	Surface heat flux
η	Dimensionless variable
D_T	Thermophoresis diffusion coefficient
$u,\, v,\, w$	Velocity components
Fig.	Figure
θ	Dimensionless temperature
q_w	Surface heat flux
3D	Three dimensional
HAM	Homotopy analysis method
ANN-LMM	Artificial Neural Network Model with Levenberg Marquardt method
τ	Cauchy stress tensor
R_1	Rivlin-Erickson tensor
λ_2	Retardation time
μ	Dynamic viscosity
b	Relative stretching parameter
A	Stretching coefficient
σ	Electric conductivity parameter
B	Magnetic field parameter
T	Temperature
q	Heat flux
λ	Thermal relaxation factor
T_W	Surface temperature
M	Magnetic field parameter
β	Deborah number
f	Dimensionless stream function
τ_{w_x}	Shear stress of the surface in horizontal direction
$C_{f_x},\, C_{f_z}$	Denotes skin friction
Nu_x	Local Nusselt number
CS	Case Study

Introduction

The significant influence of Hall current utilizing the Ohms law in hydro-magnetic (MHD) flow of non-Newtonian fluid is a recent inclination. Hall current is noticeable when the magnetic field is strong, or the density of the fluid is low because electrons carry an excited current which moves faster as compared to ions and produces an isotropic conductivity. Dynamics of fluids with Hall current effect on MHD have an extensive and broad use in the field of engineering and industries like geophysical, astrophysical space, bio-fluids, nuclear power reactor, fluid engineering and has many practical applications such as the construction of turbines, Hall sensor, Hall accelerator, centrifugal machines, MHD energy generators, control of crystal growth systems, lubrication restraint of high accelerated spinning machines, magneto astronautical flows, etc. Effect of MHD flow and Hall current inside rotating plates is reported by Shah et al. [1]. Kumar et al. [2] investigated MHD fluid flow between vertical conducting walls in the presence of the Hall effect. Opanuga et al. [3] investigated the Influence of Hall current for entropy generation of radiative MHD convective Casson fluid flow model. Akbar et al. [4] Hall current and ion slip effect on hydromagnetic biologically inspired hybrid nanofluid flow model. Awan et al. [5] examined the effect of Hall current along with electrical MHD on micropolar nanofluid. Recently, bio-heat transfer in the human body gains the reflection of numerous analysts because of its wide applications in human thermal standards which includes heat convection because of the progression of blood from the pores of tissues in a human body, radiation process among surfaces and conduction process in tissues, etc. The impact of Hall current on MHD with heat and mass transmission in a porous medium with thermal radiations was investigated by Shah et al. [6]. Chu et al. [7] examined the influence of heat transfer and radiative heat flux on Rabinowitsch. Hayat et al. [8] observed the heat transfer impacts in magneto-hydrodynamic (MHD) axisymmetric stream of third-grade liquid between the extending sheets. Riaz et al. [9] used the HAM along with a Genetic algorithm for the investigation of peristaltic transport of Jeffry fluid in a porous medium. The importance and usage of non-Newtonian fluid in the modern world of science has tremendous application in technology and industrial areas because all the rheological properties of fluid do not describe by Navier–Stokes equations. In the classification of non-Newtonian fluid Jeffery fluid is a rate type material which means it has a time derivative rather convective derivative. The Jeffrey fluid has

numerous industrial and technological applications including wire coating, dying, polymer productions, food dispensation, geophysics, chemical and petroleum, plastic manufacturing, biological fluid, etc. Sreelakshami et al. [10] present the relation of Jeffrey fluid for non-Newtonian fluids. The power-law fluid with the effect of MHD and entropy generation was studied by Khan et al. [11]. Noreen et al. [12] examined Dufour and Soret effects on Jeffrey fluid. The MHD boundary layer with Jeffrey fluid was examined by Shahzad et al. [13]. Researchers investigate a Jeffery fluid under different circumstances. Patel and Maher [14] work on the Jeffery–Hemal flow with a magnetic field. Vaidya et al. [15] look at the peristaltic Jeffery liquid with heat movement in an opposite permeable layer. Nazeer et al. [16] give the impact of non-linear thermal radioactivity on the 3D Jeffery fluid over shrinking/stretching surface in the occurrence of heterogeneous–homogeneous reactions, and injection/suction. Some potential studies about Jeffery fluid are found in these Refs. [17–20]. Asha and Sunitha [21] studied the effect of heat transfer and hall current on peristaltic blood flow on MHD with Jeffery fluid in a permeable channel. More features of Jeffery fluid with Hall current over 3D are investigated by Sinha et al. [22]. In literature, a lot of research have been done on the transportation of heat and mass theories such as enhancing the heat transfer rates and pressure loss reduction using compact heat exchanger [23]. Cattaneo model was further modified by Christov by changing time-derivative with Oldroyd-B variant [24, 25] and stability is reported in [26]. Further relevant studies on Cattaneo–Christov heat flux model (CCHFM) can be seen in [27–29]. Alamir et al. [30] work on the perspective of CCHFM. Shah et al. [31] used this model for micropolar ferrofluid on a stretched sheet. Cattaneo-Cristov heat flux model incorporated with slip condition is studied by Ahmad et al. [32]. Khan et al. [33] worked on numerical and analytical solutions of Maxwell fluid on a stretched cylinder with CCHFM.

The objective of the present research is to explore the effects of Hall current on MHD with Jeffery fluid over a nonlinear stretchable sheet. We examined the applications of Hall current on MHD with a different perspective. We analyze the characteristics of CCHFM over the variable stretchable sheet with varied thickness. In this regards, we consider the influences of heat transfer, temperature, velocity, stretching sheet with variable thickness, effects of the electric field, induced magnetic field, Hall current parameter, Jeffery parameters, Deborah number, Nusselt number, skin friction coefficient, shear stress are computed. Mathematical modeling will be presented to construct the nonlinear coupled ordinary differential equations. Similarity transformations are applied and transformed governing equations using Adams Bash-forth method. Further, the experimental data will be analyzed using the Artificial Neural Network model

with the Levenberg Marquardt method (ANN-LMM). Artificial intelligence techniques-based stochastic approaches are based on machine learning mechanism which works on the pattern of human behavior to find the stiff and valuable solutions to various types of important problems related to face identification, device management system, radar assembling, cancer diagnostic mechanism, and virus deification. The main components in the intelligent system work with the setting and adjustments of neurons and layers which play a vital and significant role for the best modeling of the designed networks and for their optimizations through different local and global heuristics. system etc. Robbins and Monro [34] analyzed intelligent computing infrastructure for the mathematical system. Mehmood et al. [35] examined the thermal transfer through a fluid flow via the design of a stochastic intelligent computing system. The ANN technique for heat transfer rate are analyzed by Sheikholeslami et al. [36]. An exclusive description made via investigators on this regime consists of [37–39]. Transformed governing equations are analyzed numerically using Adams Bashforth method [40–43].

Description of the fluid flow system

Consider the electrically conducted, unsteady Jeffrey fluid which passing over a stretching surface with fluctuating thickness. The stretching is by the side of the axial direction (x-axis) and y-axis which is perpendicular to the stretchable surface. The applied magnetic field $B = [0, B_0, 0]$ is taken along y axis. The low magnetic Reynold number is taken so that the induced magnetic field is negligible. The modified ohm's law by adding Hall's current effect are taken into account. The expressions of the Jeffrey model for the non-Newtonian fluids are given as:

$$\tau = -PI + \frac{\mu}{1+\lambda_1} + S \tag{1}$$

$$S = \frac{\mu}{1+\lambda_1}\left[R_1 + \lambda_2\left(\frac{\partial R_1}{\partial t} + \nabla.V\right)R_1\right] \text{ where}$$
$$R_1 = \nabla V + \nabla V^t, \tag{2}$$

where P denotes the pressure, τ be the Cauchy stress tensor, S is the stress tensor, R_1 is the Rivlin–Ericken tensor, λ_1 stands for the ratio of relaxation to the retardation times while the λ_2 is a retardation time (see Fig. 1).

Governing equations after boundary layer approximation are reduced to [5, 10, 13, 18, 28]:

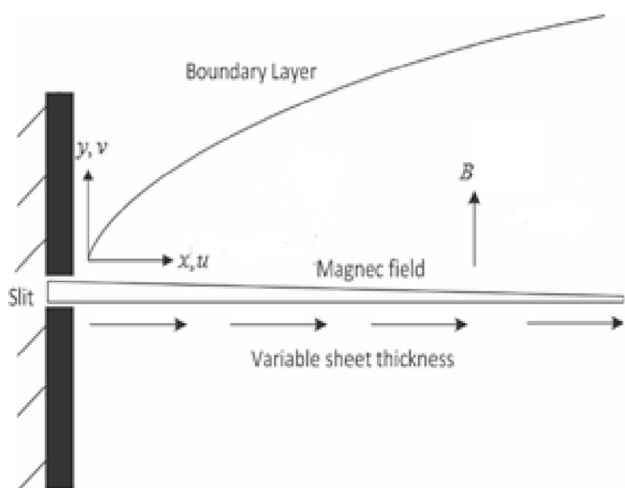$$\frac{\partial u}{\partial x} + \frac{\partial v}{\partial y} = 0, \tag{3}$$

Fig. 1 Physical configuration of the geometry

$$u\frac{\partial u}{\partial x} + v\frac{\partial u}{\partial y}$$
$$= \frac{\nu}{1+\lambda_1}\left[\frac{\partial^2 u}{\partial y^2} + \lambda_2\left\{\frac{\partial u}{\partial y}\frac{\partial^2 u}{\partial x\partial y} + u\frac{\partial^3 u}{\partial x\partial y^2} + \frac{\partial v}{\partial y}\frac{\partial^2 u}{\partial y^2} + v\frac{\partial^3 u}{\partial y^3}\right\}\right]$$
$$- \frac{\sigma B_0^2}{\rho\left(1+m^2\right)}(u+mw),$$

(4)

$$u\frac{\partial w}{\partial x} + v\frac{\partial w}{\partial y}$$
$$= \frac{\nu}{1+\lambda_1}\left[\frac{\partial^2 w}{\partial y^2} + \lambda_2\left\{\frac{\partial u}{\partial y}\frac{\partial^2 w}{\partial x\partial y} + u\frac{\partial^3 w}{\partial x\partial y^2} + \frac{\partial v}{\partial y}\frac{\partial^2 w}{\partial y^2} + v\frac{\partial^3 w}{\partial y^3}\right\}\right]$$
$$+ \frac{\sigma B_0^2}{\rho\left(1+m^2\right)}(u-mw),$$

(5)

with associated conditions

$$u = U(x) = U_o(x+b)^n,\ v = 0,\ w = 0 \quad \text{at } y = A(ax+b)^{\frac{1-n}{2}}$$
$$u \to 0, \quad w \to 0 \qquad\qquad\qquad \text{as } y \to \infty.$$

(6)

In the above expression, u, v, w and x, y represent the velocity components and Cartesian coordinates, respectively. ν represents the kinematic viscosity, μ is the dynamic viscosity and ρ is the density. The stretching rate $U(x) = U_0(x+b)^n$, with U_0 be the reference velocity, b represents the relative stretching parameter and n denotes the velocity exponent. The sheet is non-flat, and its surface is taken at $y = A(x+b)^{0.5(1-n)}$ where A is the stretching coefficient while the quantities are assumed to be constant along z-axis.

Modified Ohm's law with Hall's current effect is defined as:

$$J = \sigma\left(E + V \times B - \frac{1}{en_e}J \times B + \frac{1}{en_e}\nabla p_e\right). \quad (7)$$

Here J denotes a current density, σ denotes electric conductivity parameter, p_e is called electronic pressure parameter and B_0 denotes the magnetic field parameter. The components of J can be given as follows:

$$J_x = \frac{\sigma B_0^2}{\left(1+m^2\right)}(mu - w), \quad J_z = \frac{\sigma B_0^2}{\left(1+m^2\right)}(u + mw), \quad (8)$$

where m is the Hall parameter i-e $m = \frac{\sigma B_0^2}{en_e}$. The heat equation of steady viscous flow is defined as:

$$\rho c_p V.\nabla T = -\nabla.q. \quad (9)$$

where ρ is the density, T the temperature, c_p stands for the specific heat while q be the heat flux. Cattaneo–Christov heat flux law is defined as:

$$q + \lambda(V.\nabla q - q.\nabla V + \nabla.V)q = -\kappa\nabla.T. \quad (10)$$

Here κ represents the thermal conductivity, λ be the thermal relaxation factor. For incompressible flow

$$q + \lambda(V.\nabla q - q.\nabla V)q = -\kappa\nabla.T. \quad (11)$$

From Eqs. (9) and (10) we have

$$u\frac{\partial T}{\partial x} + v\frac{\partial T}{\partial y} = \alpha\frac{\partial^2 T}{\partial^2 y} - \lambda\left[\left(u\frac{\partial u}{\partial x} + v\frac{\partial u}{\partial y}\right)\frac{\partial T}{\partial x}\right.$$
$$+ \left(u\frac{\partial u}{\partial y} + v\frac{\partial v}{\partial y}\right)\frac{\partial T}{\partial y} + 2uv\frac{\partial^2 T}{\partial x\partial y}$$
$$\left. + u^2\frac{\partial^2 T}{\partial x^2} + v^2\frac{\partial^2 T}{\partial y^2}\right]. \quad (12)$$

Conditions for fluid temperature are

$$T = T_W \text{ at } y = A(x+b)^{\frac{1-n}{2}} \text{ and } T \to T_\infty \text{ as } y \to \infty. \quad (13)$$

The expression $\alpha = \frac{\kappa}{\rho c_p}$, T_W, T_∞ defined respective thermal diffusivity parameter, surface temperature and ambient temperature.

Similarity Conversion system

The best suitable transformation system for the presented model [44] is proved as follows:

$$u = U(x)F'(\xi) = U_0(x+b)^n F'(\xi),$$
$$v = -\sqrt{\frac{n+1}{2}\nu U_0}(x+b)^{\frac{n-1}{2}}\left[F(\xi) + \xi F'(\xi)\left(\frac{n-1}{n+1}\right)\right],$$
$$w = U(x)G(\xi) = U_0(x+b)^n G(\xi),$$

$$\Theta(\xi) = \frac{T - T_\infty}{T_w - T_\infty}, \quad \xi = y\sqrt{\frac{n+1}{2}\frac{U_0}{\nu}}(x+b)^{\frac{n-1}{2}},$$

$$\psi = F(\xi)\sqrt{\frac{2}{n+1}\nu U_0}(x+b)^{\frac{n+1}{2}}. \tag{14}$$

Using these transformations, we have:

$$F''' - (1+\lambda_1)\left[\frac{2n}{n+1}(F')^2 - FF'\right]$$
$$+ \beta\left[-\left(\frac{n+1}{2}\right)FF^{iv} + \frac{3n-1}{2}(F'')^2 + (n-1)F'F'''\right]$$
$$- \frac{2M}{(1+n)(1+m^2)}(1+\lambda_1)(F' + mG) = 0, \tag{15}$$

$$G'' - (1+\lambda_1)\left[\frac{2n}{n+1}F'G - FG'\right]$$
$$+ \beta\left[(n-1)G''F + \frac{3n-1}{2}F''G' - \left(\frac{n+1}{2}\right)FG'''\right]$$
$$+ \frac{2M}{(1+n)(1+m^2)}(1+\lambda_1)(mF' - G) = 0, \tag{16}$$

$$\Theta'' + \Pr\left[F\Theta' + \gamma\left(\frac{n-3}{2}FF'\Theta' - \frac{n+1}{2}F^2\Theta''\right)\right] = 0 \tag{17}$$

With the transformed boundary conditions:

$$F(\alpha) = \alpha\frac{1-n}{1+n}, \quad F'(\alpha) = 1, \quad G(\alpha) = 0, \quad \Theta(\alpha) = 1,$$
$$F'(\infty) = A, \quad F''(\infty) = 0, \quad G(\infty) = 0, \quad G'(\infty) = 0, \quad \Theta(\infty) = 0. \tag{18}$$

In which differentiation is with respect to ξ. We further assume the following [44]:

$$F(\xi) = f(\xi - \alpha) = f(\eta),$$
$$G(\xi) = g(\xi - \alpha) = g(\eta), \tag{19}$$
$$\Theta(\xi) = \theta(\xi - \alpha) = \theta(\eta),$$

where $\xi - \alpha = \eta$, and $\alpha = A\sqrt{\frac{n+1}{2}\frac{U_0}{\nu}}$. Then Eqs. (15)–(17) becomes:

$$f''' - (1+\lambda_1)\left[\frac{2n}{n+1}(f')^2 - ff''\right]$$
$$+ \beta\left[-\left(\frac{n+1}{2}\right)ff^{iv} + \frac{3n-1}{2}(f'')^2 + (n-1)f''f'''\right]$$
$$- \frac{2M}{(1+n)(1+m^2)}(1+\lambda_1)(f' + mg) = 0, \tag{20}$$

$$g'' - (1+\lambda_1)\left[\frac{2n}{n+1}f'g - fg'\right]$$
$$+ \beta\left[(n-1)g''f + \frac{3n-1}{2}f''g' - \left(\frac{n+1}{2}\right)fg'''\right]$$

$$+ \frac{2M}{(1+n)(1+m^2)}(1+\lambda_1)(mf' - g) = 0, \tag{21}$$

$$\theta'' + \Pr\left[f\theta'' + \gamma\left(\frac{n-3}{2}ff'\theta' - \frac{n+1}{2}f^2\theta''\right)\right] = 0 \tag{22}$$

With the transformed boundary conditions:

$$\eta = 0; \quad f(\eta) = \alpha\frac{1-n}{1+n}, \quad f'(\eta) = 1, \quad g(\eta) = 0, \quad \theta(\eta) = 1,$$
$$\eta \to \infty; \quad f'(\eta) = 0, \quad f''(\eta) = 0,$$
$$g(\eta) = 0, \quad g'(\eta) = 0, \quad \theta(\eta) = 0. \tag{23}$$

Here M denotes the magnetic field parameter, γ is the thermal relaxation parameter, β is the Deborah number, Pr is the Prandtl number, α is the thermal diffusivity and m is the Hall parameter. In boundary conditions α is the wall thickness parameter, η corresponds to the surface of the sheet which non-dimensional similarity variable, f is the dimensionless stream function, T is the temperature of the fluid, T_W is the surface temperature, T_∞ is the ambient temperature. θ is the dimensionless temperature. where prime denotes the derivative with respect to η. Parameters involved in the non-dimensional equations are:

$M = 2\sigma(x+b)^n B_0^2 / \rho U(x)$ represent the magnetic field parameter, $\Pr = \rho c_p \nu / k$, represents Prandtl number $\gamma = \lambda U_0(x+b)^{n-1}$ is the thermal relaxation parameter, $\alpha = A\sqrt{(n+1)U_0/2\nu}$ is wall thickness parameter where $A = y(x+b)^n$ and $\beta = \lambda_2 A_1$ is the Deborah number where $A_1 = \gamma/\lambda$.

Skin friction factor and Nusselt number

The skin friction coefficient at the stretched surface is written as:

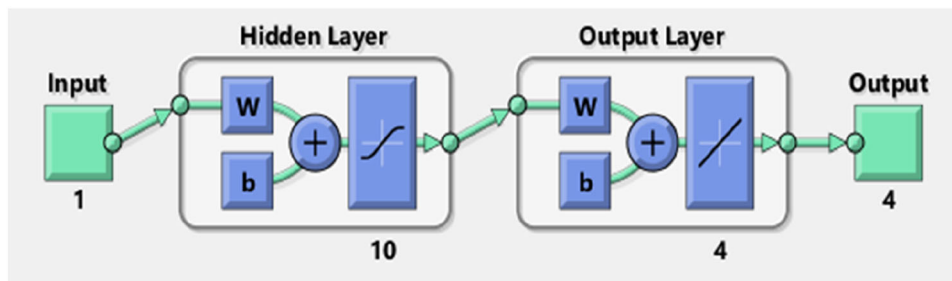$$C_{fx} = \frac{\tau_{w_x}}{\rho u_w^2}, \quad \text{where}$$

$$\tau_{w_x} = \frac{\mu}{1+\lambda_1}\left[\frac{\partial u}{\partial y} + \lambda_2\left(u\frac{\partial^2 u}{\partial x \partial y} + v\frac{\partial^2 u}{\partial y^2}\right)\right]_{y=A(x+b)^{\frac{1-n}{2}}}, \tag{24}$$

$$C_{fz} = \frac{\tau_{w_z}}{\rho u_w^2}, \quad \text{where}$$

$$\tau_{w_z} = \frac{\mu}{1+\lambda_1}\left[\frac{\partial w}{\partial y} + \lambda_2\left(u\frac{\partial^2 w}{\partial x \partial y} + v\frac{\partial^2 w}{\partial y^2}\right)\right]_{y=A(x+b)^{\frac{1-n}{2}}}. \tag{25}$$

Here τ_{w_x}, τ_{w_z} are shear-stress of the surface in the horizontal direction and shear stress is perpendicular to the

Fig. 2 Basic structure of ANN model with 10 hidden layers

horizontal direction, accordingly. Dimensionless form is:

$$C_{f_x}\text{Re}_x^{1/2} = \frac{1}{1+\lambda_1}\left[f'' + \beta\left(\frac{3n-1}{2}f'f'' - \frac{n+1}{2}ff'''\right)\right] \tag{26}$$

$$C_{f_z}\text{Re}_x^{1/2} = \frac{1}{1+\lambda_1}\left[g' + \beta\left(\frac{3n-1}{2}f'g' - \frac{n+1}{2}fg''\right)\right] \tag{27}$$

where C_{f_x}, C_{f_z} denotes skin friction $\text{Re}_x = \frac{(x+b)U(x)}{v}$ is the Local Reynold number.

The heat transfer rate relations are written as follows:

$$\text{Nu}_x = \frac{xq_w}{k(T_w - T_\infty)}, \quad q_w = -k\left.\frac{\partial T}{\partial y}\right|_{y=A(x+b)^{\frac{1-n}{2}}} \tag{28}$$

Here q_w is the surface heat flux. Non-dimensional form is:

$$\text{Nu}_x\text{Re}^{-1/2} = -\sqrt{\frac{1+n}{2}}\theta''(0), \tag{29}$$

where Nu_x represents the local Nusselt Number.

Structure of the designed intelligent network

Stat of the art Adams Bash-forth numerical method is incorporated with the assistance of ND-Solve command exploited through Mathematica software. The considered numerical is the best suitable numerical computing technique for the generation of the dataset for further designing of the artificial neural networks. The diagram of the designed intelligent network is described in Fig. 2.

The above-mentioned network is a mathematical system inspired by biological neural networks, which is dependent upon the collection of neurons. Neurons are the integral and important component of the designed soft computing-based intelligent network that transformed the data obtained through any deterministic-based method like Adam's numerical method and then gives the result in the output layer. Data traveled from the input layer to the layer connected with

the output setting of the network. Different layers are also incorporated into the designed networks for finding the best possible outcomes. The total data set is classified into 70% training, 15% validation, 15% testing. The present article carries out the Hall current with Jeffrey fluid and CCHFM. In this regards the experimental data will be analyzed by using the Artificial Neural Network model with Leven-berg Marquardt method (ANN-LMM).

Numerical results and discussion

In a current research article, reference numerical result and ANN is applied for the estimate of the Hall effect on MHD flow with Jeffrey fluid and heat transfer with CCHFM. Numerical solutions with the help of ND-Solve command and Artificial Neural Network (ANNs) are investigated. Table 1 is constructed for all variants of the presented MHD flow of the Jeffrey fluid system under the impact of heat. Velocity profile $f'(\eta)$ is represented through case study 1, and another velocity profile $g(\eta)$ is shown via case study 2, whereas case study 3 represents the temperature profile $\theta(\eta)$. Scenarios 1, 2, 3 denotes the variables. Scenarios 1, 2 and 3 of case study 1 represent the Hall current parameter (m), wall thickness parameter (α), ratio of relaxation to the retardation time (λ_1). Case study 2 is about Hall current parameter (m), Deborah number (β). Case study 3 represents the thermal relaxation parameter (γ), Prandtl number (Pr.), velocity exponent parameter (n).

### Performance analysis of numerical solution:

We obtained the non-dimensional velocities and temperature profiles for emerging parameters. Using ND-solve command in MATHEMATICA software with ADAM BASHFORTH method, we obtained solutions for profiles $f'(\eta)$, $g(\eta)$ and $\theta(\eta)$ for various cases. Figures 3, 4 and 5 investigate the impact of parameter m, M, λ_1 with the ranges $0.3 \leq m \leq 0.12$, $0.0 \leq M \leq 1.5$, $0.0 \leq \lambda_1 \leq 0.12$ for $f'(\eta)$. Figure 3 indicates the behavior of hall current parameter (m). The velocity profile $f'(\eta)$ increases for a large value of $0.3 \leq m \leq 0.12$ because the effect of electric conductivity of

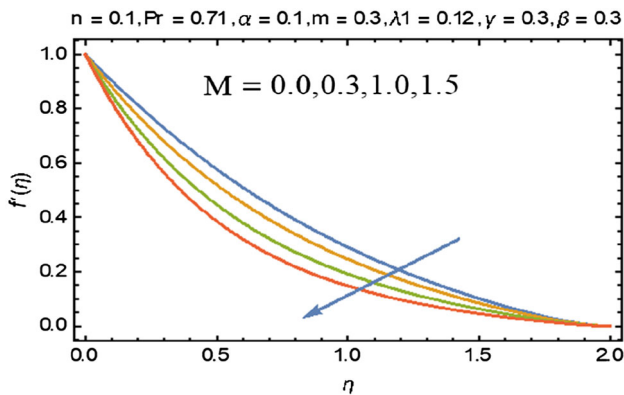**Table 1** Values of parameters associated with the fluid flow system

Case study	1			2		3		
Scenario	1	2	3	1	2	1	2	3
Case: 1	0.3	0.0	0.0	0.1	0.3	0.2	0.71	0.1
Case: 2	0.6	0.3	0.4	0.3	0.4	0.6	1.0	0.3
Case: 3	0.9	1.0	0.8	0.6	0.6	0.7	1.5	0.6
Case: 4	0.12	1.5	0.12	0.9	0.8	0.8	2.0	0.9
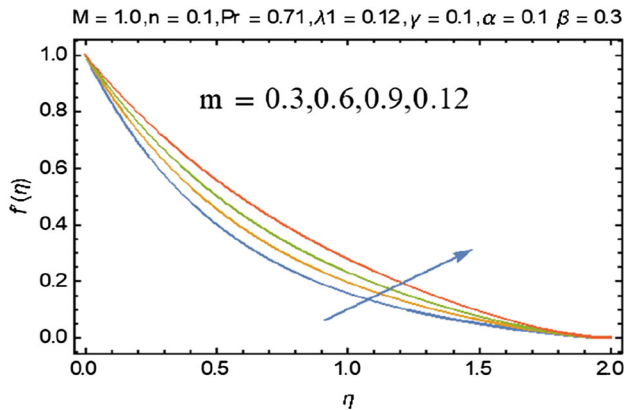
Fig. 3 Plot representing Scenario (m) for case study 1
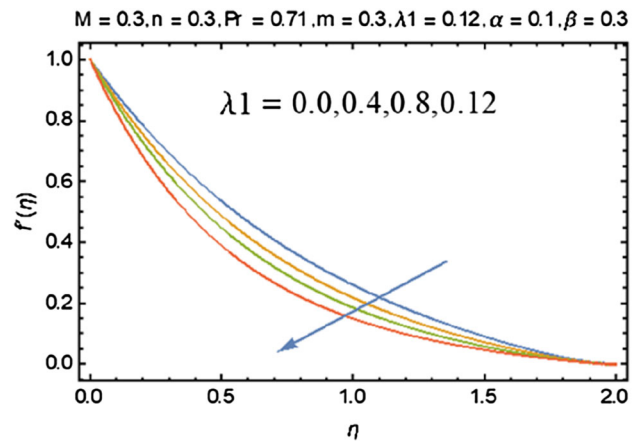
Fig. 5 Plot representing Scenario (λ_1) for case study 1

Fig. 4 Plot representing Scenario (M) for case study 1
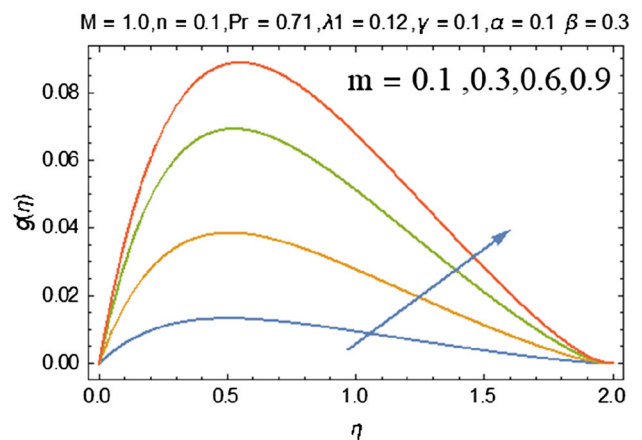
Fig. 6 Plot representing Scenario 1 (m) for case study 2

the fluid enhances the molecular movement which results in an increase in fluids velocity. According to this relation $\sigma/(1 + m^2)$, effective conductivity decreases when we increase the values of m. By increasing the Hall current parameter m, the factor $1/(1 + m^2)$ becomes smaller so the resistivity of the fluid decreases whereas it shows the same behavior in the case of velocity profile $g(\eta)$ which is observed in Fig. 6. When we increase the value of Hall current parameter m, the velocity profile also increases. Figure 4 shows the impact of the magnetic field parameter (M). When we increase the value of M the velocity component $f'(\eta)$ shows a reduction. This is due to the fact that magnetic field M induces

the resistive force which is also called a Lorentz force while the velocity profile reduces because when the Lorentz force becomes weaker, the motion of the fluid reduces and the fluid become to rest. It is because of the fact the magnetic field acts as retarding/controlling agent and has the ability to control the fluids velocity upto desired value. Figure 5 influences the ratio of relaxation to the retardation time λ_1 on the velocity profile $f'(\eta)$ along with the boundary layer because the physical ratio of relaxation to the retardation time depends upon the retardation time. As λ_1 increases the relaxation time and
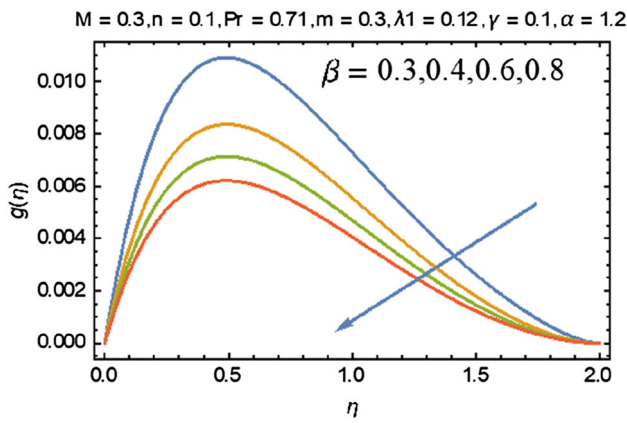
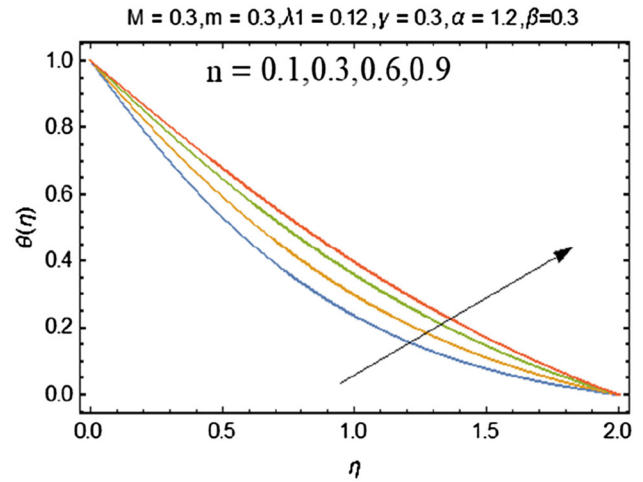**Fig. 7** Plot representing Scenario (β) for case study 2

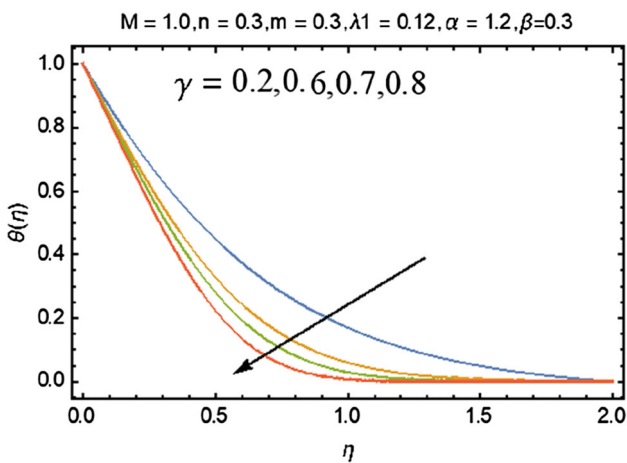
Fig. 8 Plot representing Scenario (γ) for case study 2

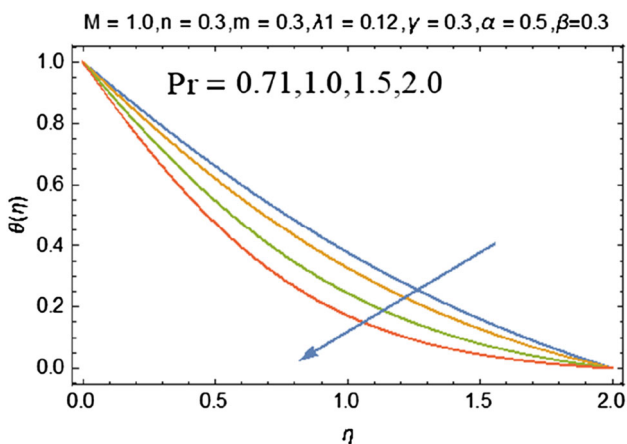**Fig.9** Plot representing Scenario (Pr.) for case study 3

Fig. 10 Plot representing Scenario (n) for case study 3

it reduces the retardation time. Jeffrey fluid parameter was the reason for the variation of the momentum boundary layer, so the velocity reduces in the variable sheet. Figure 7 exhibit the effect of Deborah number β on the velocity profile $g(\eta)$. As it was observed from Fig. 7 that for the larger value of the Deborah number β, velocity profile $g(\eta)$ reduces. Physically, Deborah number depends upon retardation time so with the enhancement of the retardation time Deborah number decreases but it increases for the gradient of the velocity profile of the Jeffrey fluid. Figures 8, 9 and 10 exhibit the influence of γ, Pr, n with the ranges $0.2 \leq \gamma \leq 0.8$, $0.71 \leq$ Pr. ≤ 2.0, $0.1 \leq n \leq 0.9$ respectively on the temperature profile $\theta(\eta)$. Figure 8 shows that an increment in the value of thermal relaxation parameter γ results into a reduction of the temperature profile $\theta(\eta)$ because the temperature of variable sheet decreases with the enhancement of the thermal relaxation γ. In case when the thermal relaxation parameter reduces to zero i-e ($\gamma = 0$) the CCHFM becomes the classical Fourier law of heat conduction. Figure 9 presents the impact of Prandtl number Pr. On the temperature profile $\theta(\eta)$.it is observed from the figure that the temperature profile $\theta(\eta)$ reduces for the larger values of Pr. Number. Physically, the Prandtl number depends upon the thermal diffusivity and thermal diffusivity becomes lower with the enhancement of the Prandtl fluid because of the fluid with high pr. number shows less conduction. Due to this reason when we increase the value of pr. number thermal diffusivity reduced and temperature profile reduces. Figure 10 demonstrated the influence of the velocity exponent parameter (n) on $\theta(\eta)$. For the larger n, the profile $\theta(\eta)$ increases. The positive value of n i-e ($n > 0$) shows that the variable sheet is stretching. For the transverse velocity distributions, it shows the same behavior. Variation for M, Pr., α, λ_1, m, γ, β of and skin friction coefficient and Nusselt number are presented in Table 2.

Performance analyses on outcomes of the networks

The elaborative numerical solution of transformed system of ODEs by ANN is presented for various parameters of profiles $f'(\eta)$, $g(\eta)$ and $\theta(\eta)$. Solution by ANN with Levenberg Marquardt method (ANN-LMM) interpreted through error histogram, plot fit, training states, performance and regression. Performances of three scenarios of all the cases of case study 1, 2 and 3 are presented. Result will be analyzed by comparison.

Case study 1

The performances of 3 scenarios (m, M, λ_1) for case study 1 (CS1) for different $f'(\eta)$ are illustrated in Figs. 11, 12, 13, 14, 15, 16, 17, 18, 19, 20, 21, 22, 23, 24 and 25. Sub-Fig. 11a–c present the error histogram which exhibits the data fitting error for all the cases which are near to zero error reference line. More positive error is exhibited for case 1 whereas negative error for case 2 and case 3. Figure 12a–c delineate the data of fitness based on difference between the target and network outputs after training a neural network, i.e., the difference between the predicted value and target value. The range of the absolute zero in three cases of scenario 1 is $(-2 \times 10^{-4}$ to $2 \times 10^{-4})$. The error is found to be very close to zero which shows the fitness of the method with good accuracy. Means square error (MSE) of three cases of scenario 1 is illustrated in sub-Fig. 13a–c. Minimum of MSE is achieved at epoch (349, 66, 264) with respective best validation performance $(8.2625e^{-10}, 3.15671e^{-10}, 1.5309e^{-9})$. Figure 14a–c present algorithm execution states of the networks. Training states describe the outcomes of controlling indices of Mu and gradient. For all the cases best validation performance depends upon epoch weights. The values of the gradient for all the cases at (349, 66, 264) are given respective as $(9.96e^{-8}, 9.51e^{-8}, 9.99e^{-8})$ that verified networks performance. Sub-Figure 15a–c gives the regression plots of the data for different outputs. The regression measure, i.e., correlation R = 1, exhibits a strong correlation consistently.

Figures 16, 17, 18, 19 and 20 describe the interpretation of three cases of scenario 2 of case study 1 (CS1) graphically. Figure 16a–c portray plots for the error histogram studies. The error is consistently close to reference with higher error for cases 1 and 2 and relatively less for case 3 which shows the reasonable performance. Sub-Figure 17a–c present the fitness plots. Interval of the absolute error with the ranges $(-5 \times 10^{-4}$ to 5×10^{-4}, -2×10^{-4} to 2×10^{-4}, -5×10^{-4} to $5 \times 10^{-4})$ respectively are analyzed which are close to zero. Figure 18a–c demonstrate the MSE for all the cases of scenario 2. The MSE gradually decreases with epochs, it is observed at epoch (73, 89, 298) with the best respective validation performance are $(1.33312e^{-8}, 6.41000e^{-10}, 9.79812e^{-10})$. Training states depend upon

Mu, gradient and validation check as shown in Fig. 19a–c. The magnitude of the gradient $(1.78e^{-5}, 9.99e^{-8}, 9.99e^{-8})$ at (73, 89, 298). The sub-Fig. 20a–c present the regression plots with a value of R = 1 for scenario 2 consistently for each dataset of the model.

Performance analysis of ANNs model for each variation of scenario 3 is graphically provided in Figs. 21, 22, 23, 24 and 25. The sub-Fig. 21a–c displayed the error histograms of scenario 3 for three cases. The data set points with an error close to zero having less errors for cases 1 and 3 whereas bit more errors for case 2. The sub-Fig. 22a–c present the fitness plots which show that the error is close to zero i.e., the predicted value suits to experimental data values. The error for all the cases lies in the range of $(-2 \times 10^{-4}$ to 2×10^{-4}, -1×10^{-5} to 1×10^{-5}, -2×10^{-4} to $2 \times 10^{-4})$. Figure 23 demonstrated the performance analysis graphically After training the data set the least value of MSE is obtained. The best validation performance at epochs (284, 293, 249) is given as $(1.6407e^{-9}, 22.23755e^{-11}, 8.87428e^{-10})$ which shows that the data set is well trained. Further, the training states give Mu, gradient, validation checks observed in Fig. 24a–c. The gradient is $(9.96e^{-8}, 9.97e^{-8}, 9.83e^{-8})$ for the three cases of scenario 3 which gives consistently viable results. Additionally, the value of Mu $(1e^{-9}, 1e^{-9}, 1e^{-9})$ is found close to zero for scenario 3 in each case. Sub-Figure 25a–c also show the regression analysis of the predicted and target value of scenario 3 with regression index R = 1 that presents the rationality of the accurate performance of the ANN network model.

Case study 2

The analysis of networks for velocity profile $g(\eta)$ of different scenarios for various emerging parameters of case study 2 (CS2) are illustrated in Figs. 26, 27, 28, 29, 30, 31, 32, 33, 34 and 35. Figure 26a–c depicts accurately our model through the prediction of the data set after training. Higher positive error exhibits for case 1 and negative error for cases 2 and 3. Figure 27a–c demonstrates the fitting plots graphically for scenario 1 of three cases. Absolute errors for the presented fluid system show good performance analysis as its most of the values lie in the ranges $(-5 \times 10^{-5}$ to 5×10^{-5}, -2×10^{-4} to 2×10^{-4}, -1×10^{-4} to $1 \times 10^{-4})$ respectively with better precision. The sub-Fig. 28a–c presents the performance analysis with the best validation performance of the given data set for three cases of scenario 1. The minimum value of MSE are $(1.57918e^{-10}, 1.41400e^{-10}, 2.98581e^{-10})$ at the epoch (12, 21, 39) with good validation. The sub-Fig. 29a–c depict the training states of all variants associated with scenario 1. The magnitudes of the gradient $(6.14e^{-8}, 9.60e^{-8}, 9.35e^{-8})$ at the epoch (12, 21, 39). Further, the value of Mu for all the cases of scenario 1 is $(1e^{-12}, 1e^{-11}, 1e^{-11})$ which shows the convergence of the ANN

Table 2 Outcomes on Skin friction coefficients $-C_{fx}\mathrm{Re}_x^{0.5}$, $C_{fz}\mathrm{Re}_x^{0.5}$ and local Nusselt number $\mathrm{Nu}_x\mathrm{Re}^{-0.5}$ various values of parameters

M	Pr	α	λ_1	m	γ	β	$-C_{fx}\mathrm{Re}_x^{0.5}$	$C_{fz}\mathrm{Re}_x^{0.5}$	$Nu_x\mathrm{Re}^{-0.5}$
0.1	0.71	0.1	0.12	0.1	0.1	0.3	0.882806	0.00867397	0.499076
0.5							1.76644	0.0350695	0.490395
1.0							1.48126	0.0573754	0.48217
1.5							1.7403	0.0739294	0.475888
0.5	0.71						1.17644	0.0350695	0.490395
	1.0						1.17644	0.0350695	0.542903
	1.5						1.17644	0.0350695	0.636657
	2.0						1.17643	0.0350695	0.732635
0.5	0.71	0.1					1.17644	0.0350695	0.490395
		0.5					1.41977	0.0363513	0.588698
		1.0					1.75384	0.0370208	0.735939
		1.5					2.1108	0.0371283	0.917479
0.5	0.72	0.1	0.11				1.17674	0.352166	0.491761
			0.15				1.15536	0.0347679	0.491071
			0.18				1.14012	0.0344409	0.490563
			0.21				1.12552	0.0341218	0.490064
			0.12	0.1		0.3	1.17644	0.0350695	0.490395
				0.3			1.15457	0.0990267	0.490964
				0.6			1.09684	0.165504	0.492517
				0.9			1.03398	0.195308	0.494294
					0.1		1.17644	0.350695	0.490395
					0.5		1.17644	0.350695	0.467594
					1.0		1.17644	0.350695	0.43867
					2.0		1.17644	0.0350695	0.379288
0.3		1.2		0.3	0.1	0.1	1.63931	0.0622123	0.803698
						0.3	1.73033	0.0665242	0.806509
						0.5	1.81492	0.0694501	0.808414
						0.8	1.93405	0.0723667	0.810269

(a) Case:1   **(b) Case:2**   **(c) Case:3**
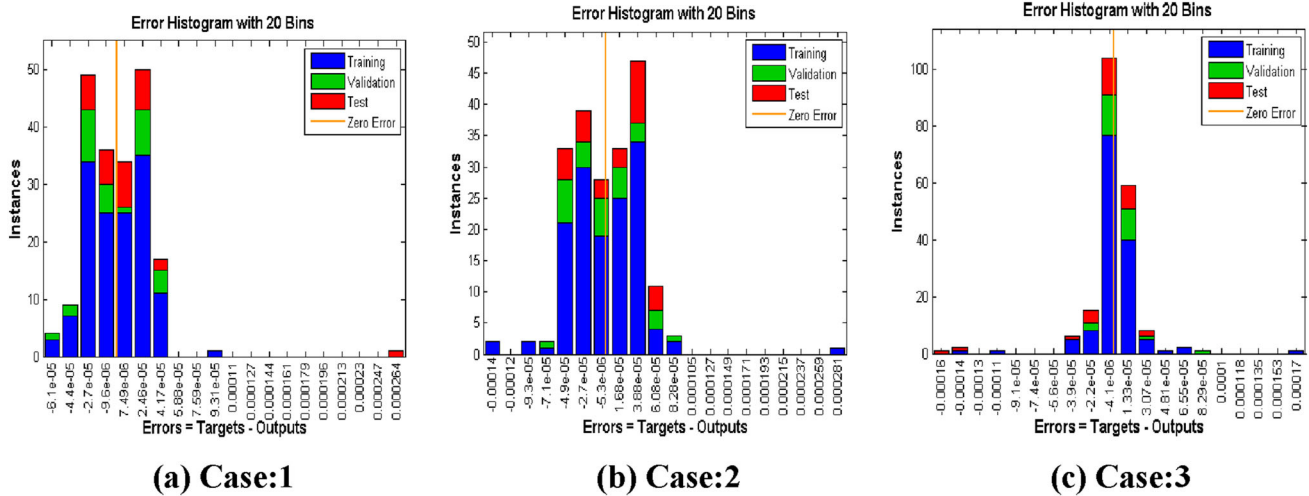
Fig. 11 Error histogram of Scenario 1. **a** Case: 1, **b** Case: 2, **c** Case: 3
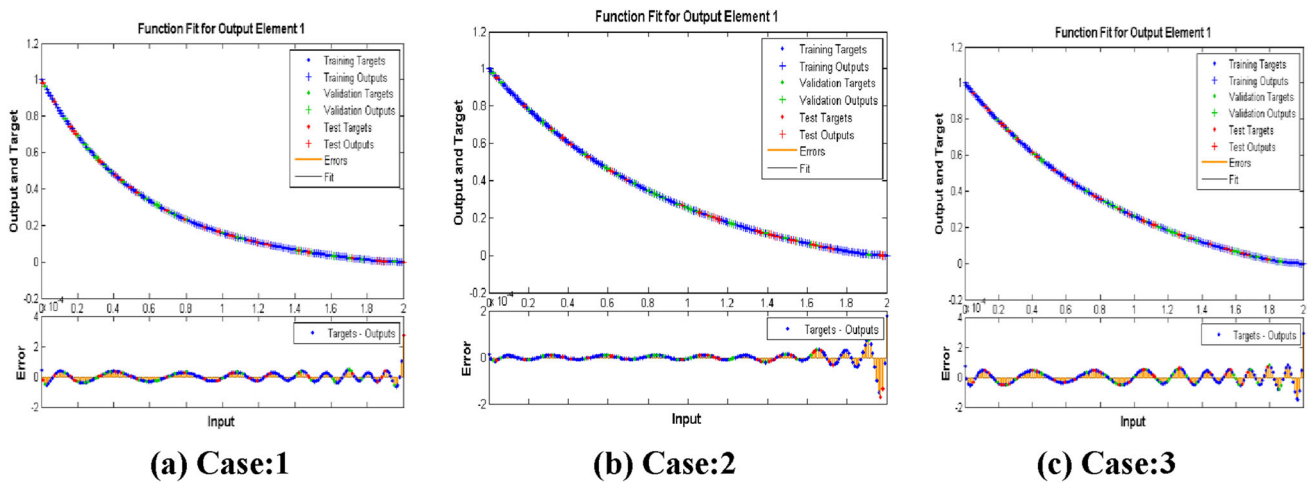
Fig. 12 Plot fit of scenario 1. **a** Case: 1, **b** Case: 2, **c** Case: 3
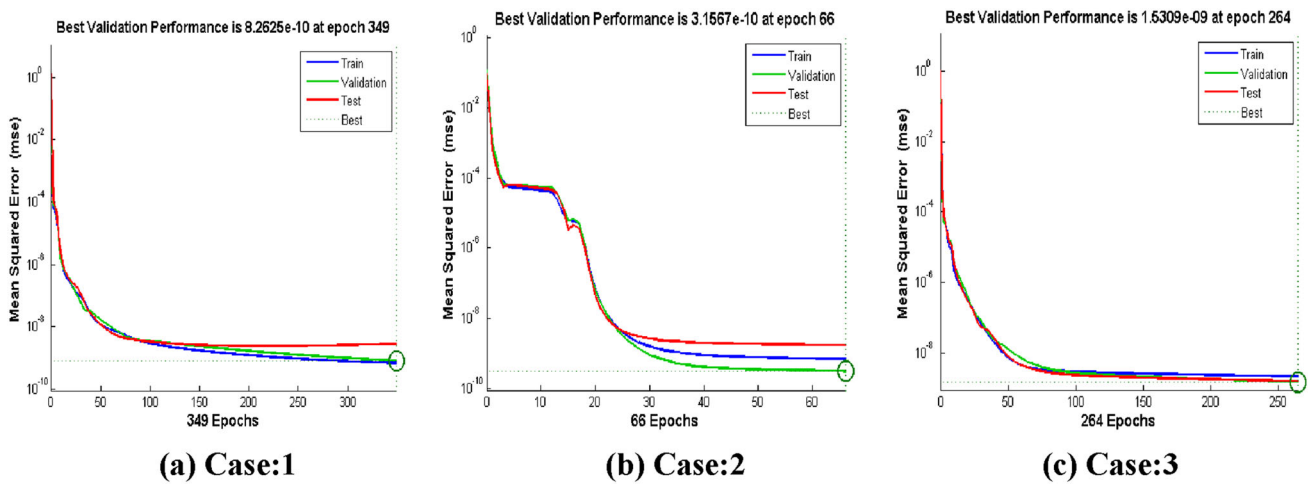
Fig. 13 Performance curve of scenario 1. **a** Case: 1, **b** Case: 2, **c** Case: 3
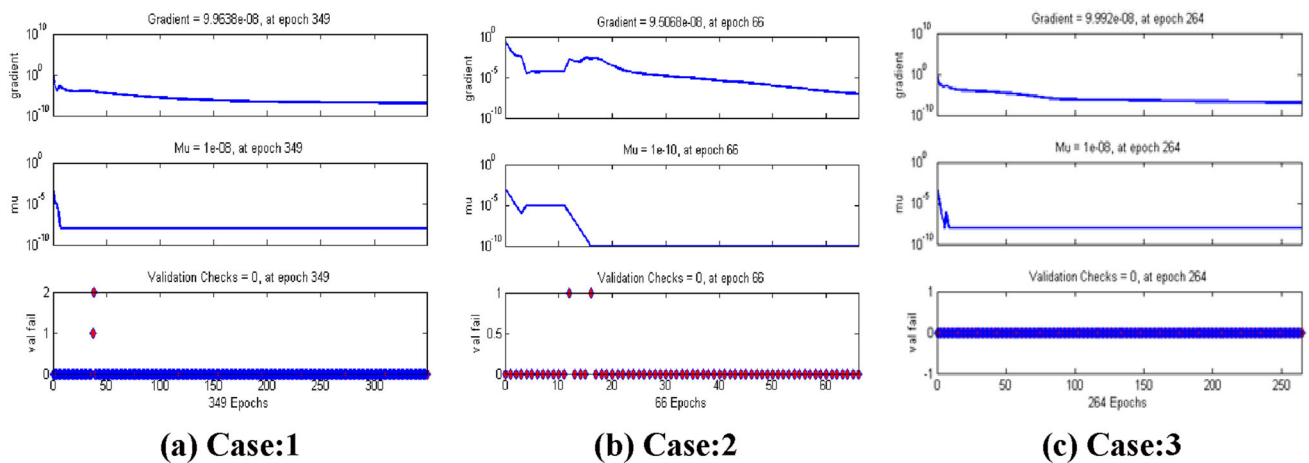
Fig. 14 Training state of scenario 1. **a** Case: 1, **b** Case: 2, **c** Case: 3
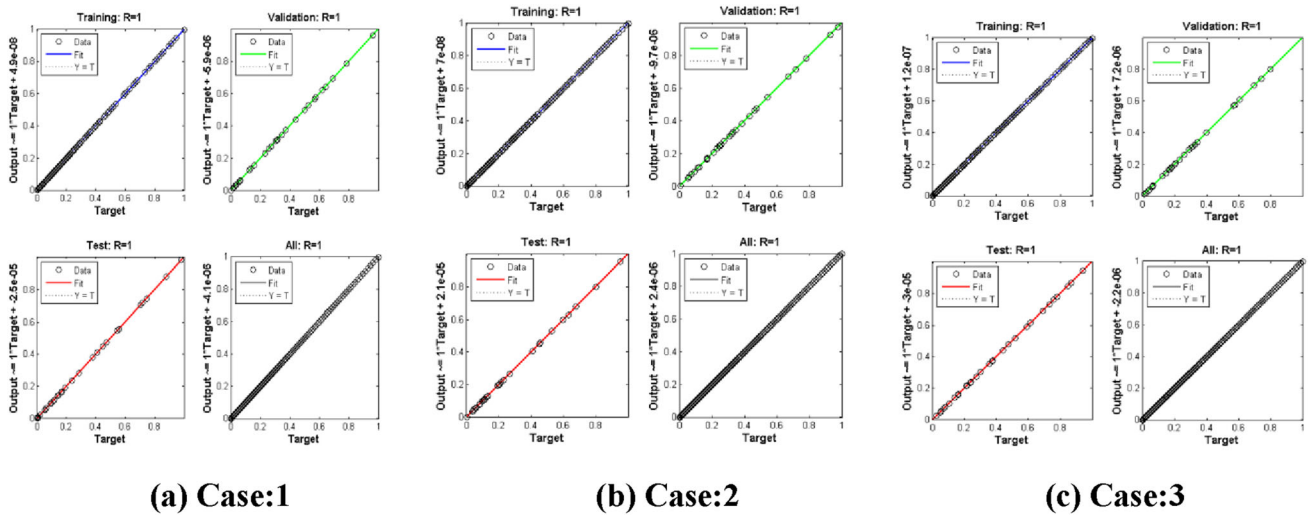
Fig. 15 Regression plot of scenario 1. **a** Case: 1, **b** Case: 2, **c** Case: 3
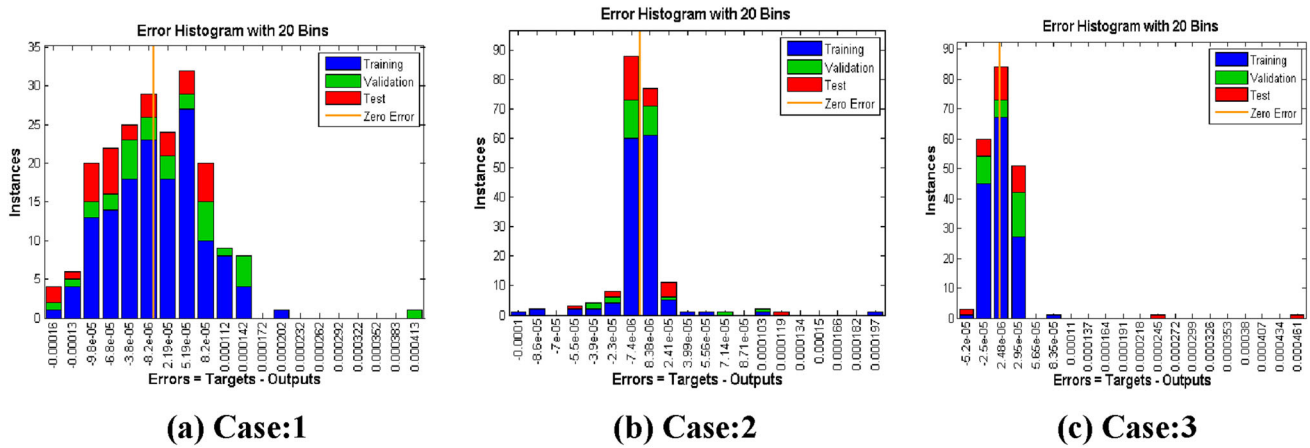
Fig. 16 Error histogram of scenario 2. **a** Case: 1, **b** Case: 2, **c** Case: 3
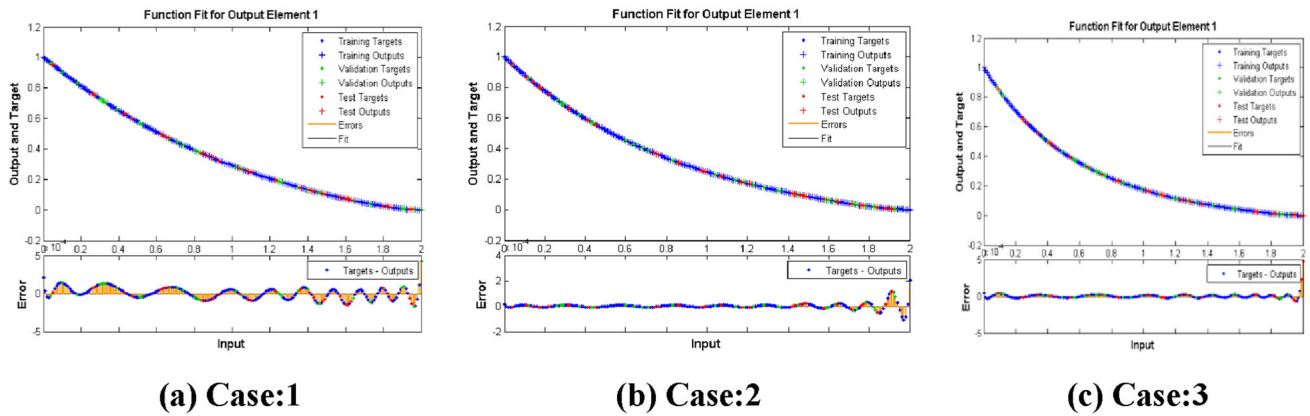
Fig. 17 Plot fit of scenario 2. **a** Case: 1, **b** Case: 2, **c** Case: 3
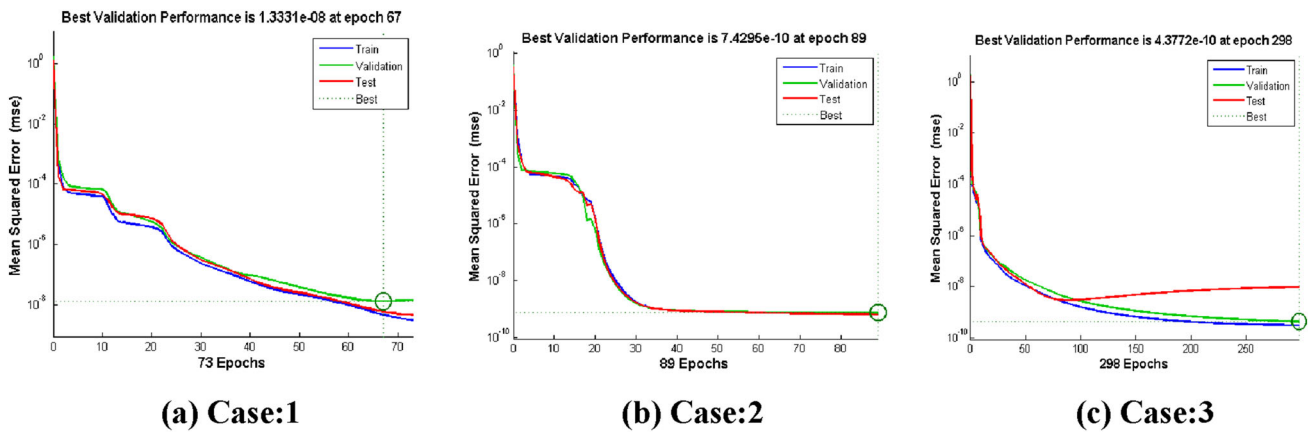
Fig. 18 Performance curve of scenario 2. **a** Case: 1, **b** Case: 2, **c** Case: 3
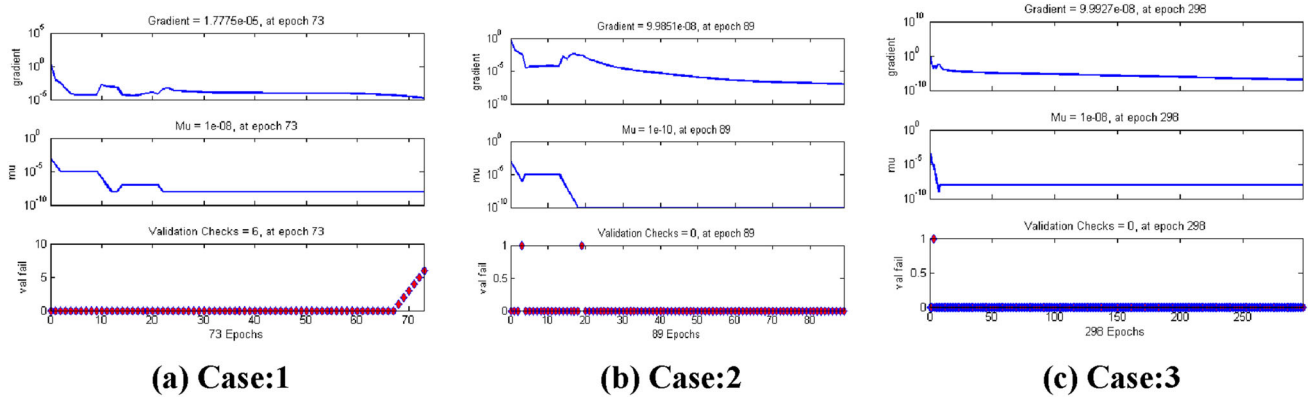
Fig. 19 Training state of scenario 2. **a** Case: 1, **b** Case: 2, **c** Case: 3
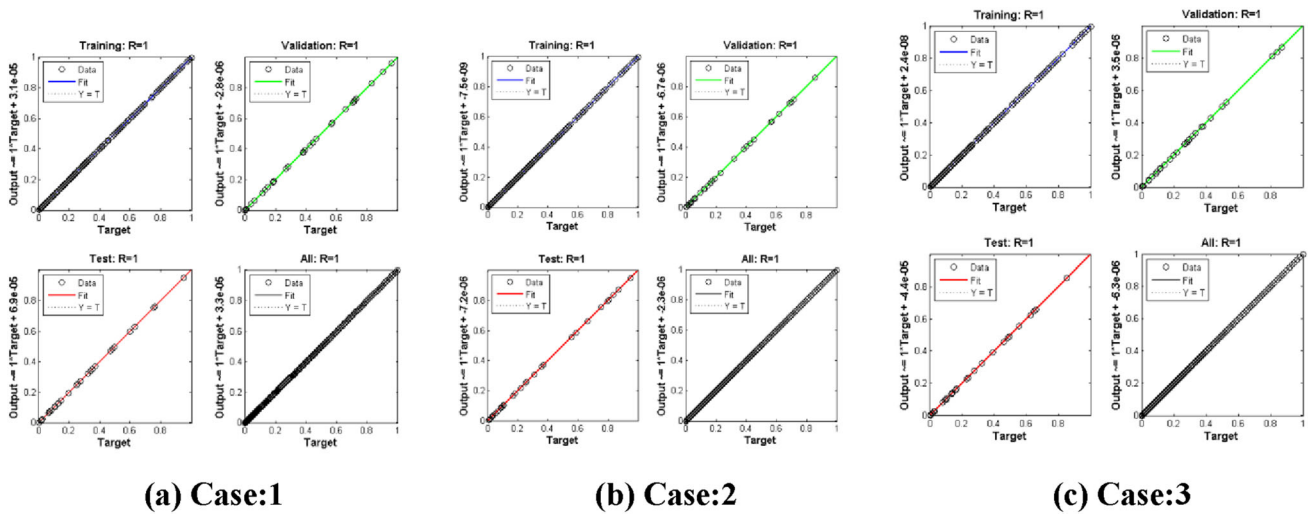
Fig. 20 Regression plot of scenario 2. **a** Case: 1, **b** Case: 2, **c** Case: 3
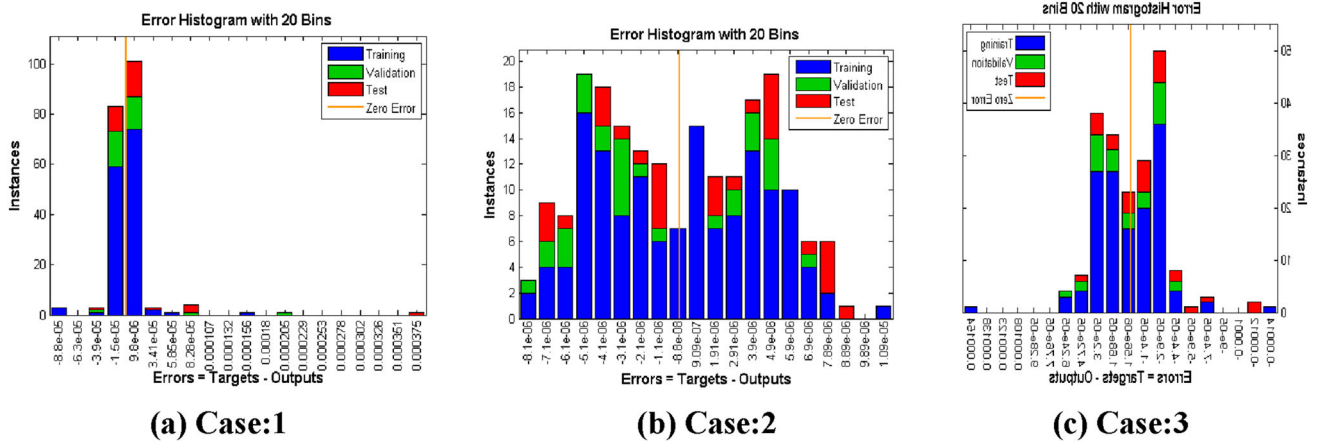
Fig. 21 Error Histogram of scenario 3. **a** Case: 1, **b** Case: 2, **c** Case: 3
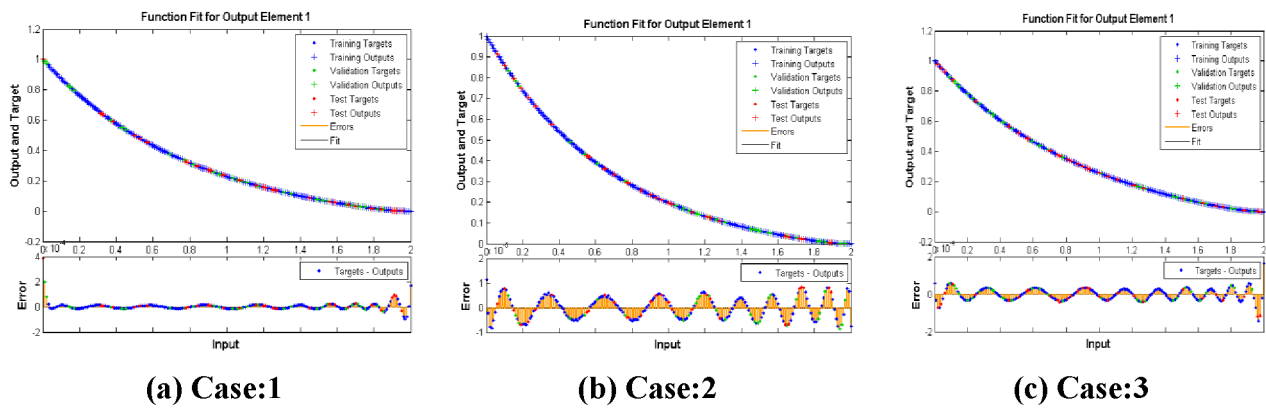
Fig. 22 Plot fit of scenario 3. **a** Case: 1, **b** Case: 2, **c** Case: 3
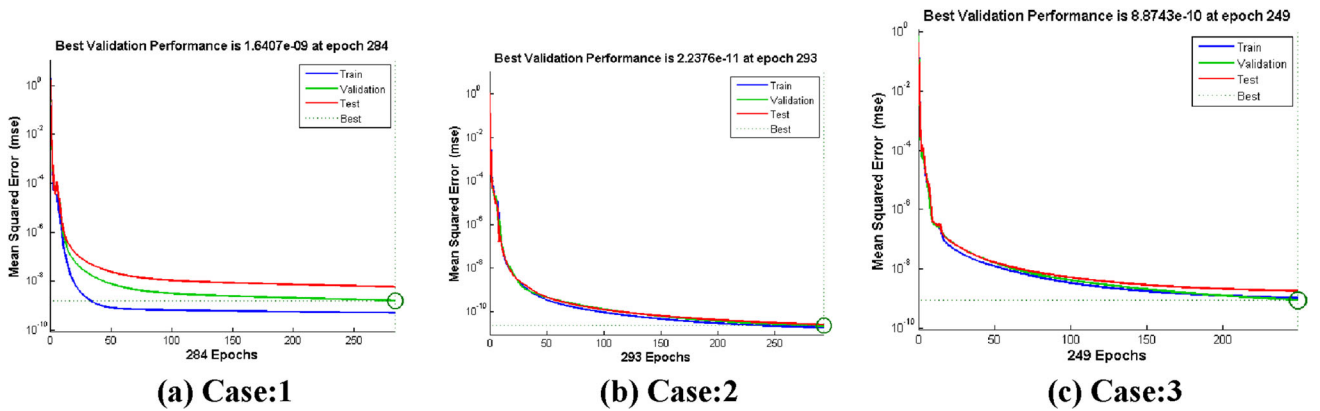
Fig. 23 Performance curve of scenario 3. **a** Case: 1, **b** Case: 2, **c** Case: 3

model. Figures 30a–c presents the regression metric R = 1 for the three cases of scenario 1 with good accuracy of the ANN model.

Figures 31, 32, 33, 34 and 35 influence the scenario for three cases of case study 2 (CS2) Fig. 31a–c depicts that most of the values give reasonable accuracy for case 1, whereas higher negative zero error for case 2 and 3. Figure 32 shows

the plot fitness of all variants associated with scenario 1. The error was found close to (-2×10^{-4} to 2×10^{-4}) for all the cases. Figure 33a–c shows the mean square error and the best validation performance at epoch (7, 9, 9) are given ($6.29335e^{-9}$, $1.96818e^{-9}$, $2.22200e^{-9}$), respectively, which shows that the data set is well trained. Moreover,
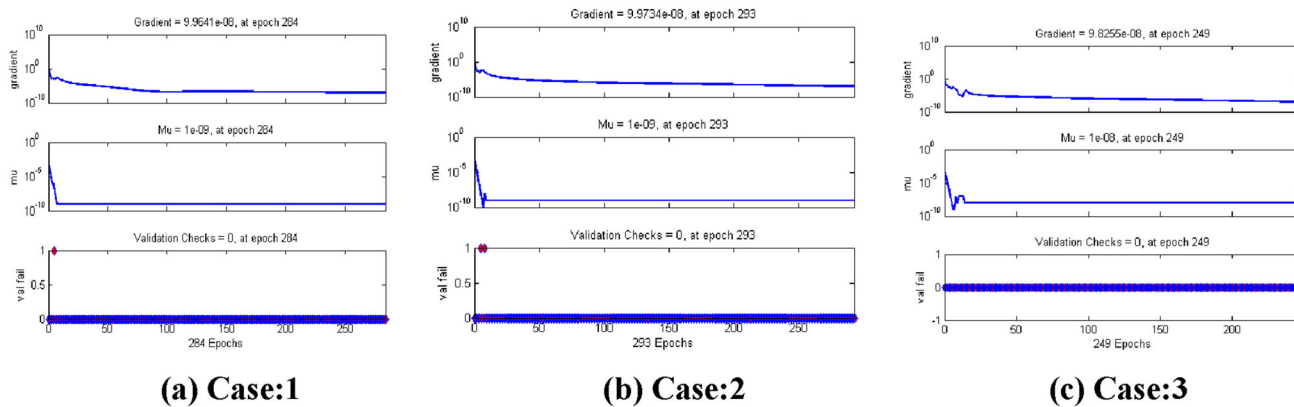
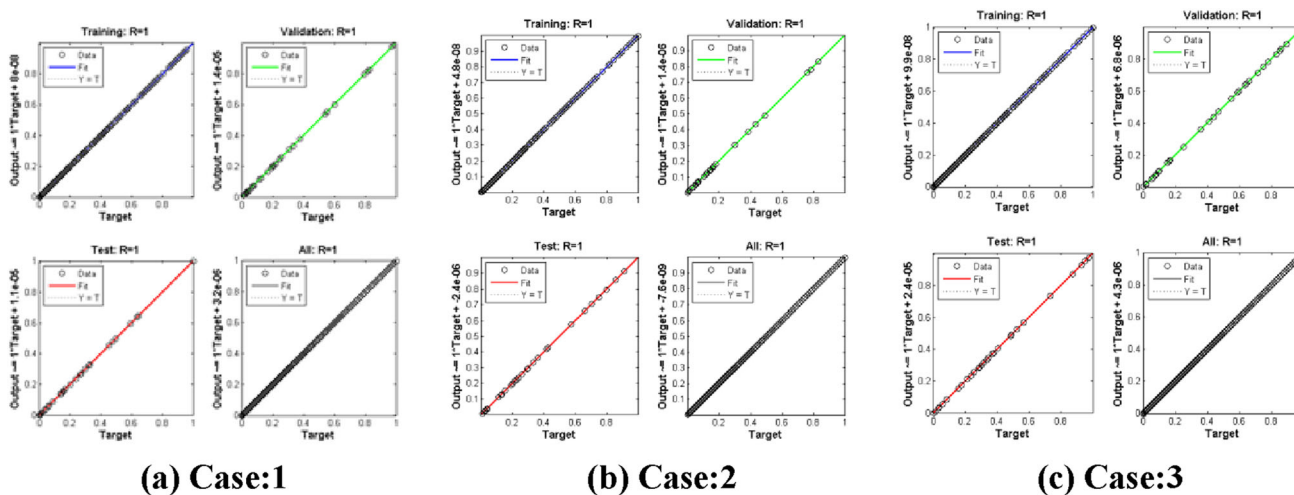**Fig. 24** Training state of scenario 3. **a** Case: 1, **b** Case: 2, **c** Case: 3

Fig. 25 Regression plot of scenario 3. **a** Case: 1, **b** Case: 2, **c** Case: 3
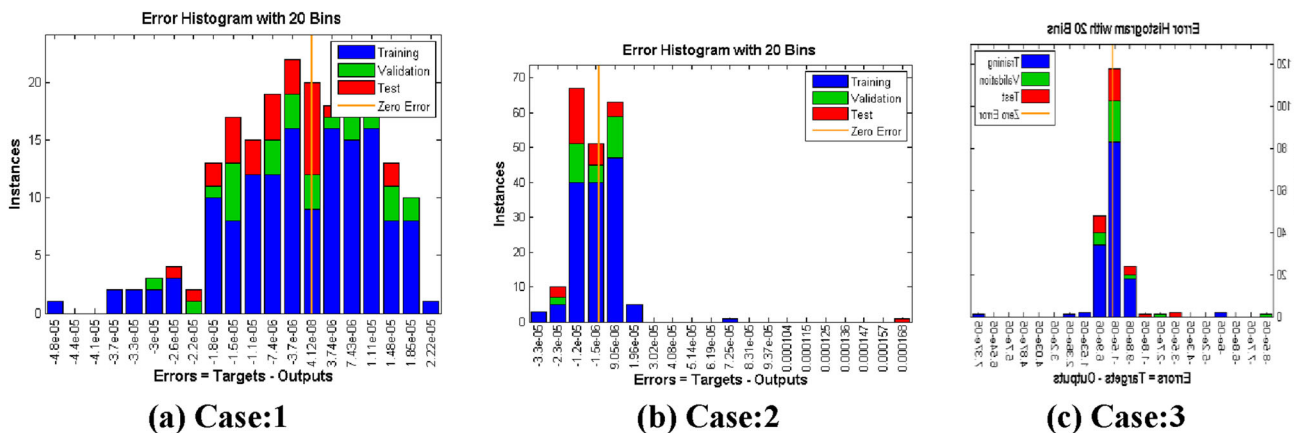
Fig. 26 Error histogram of scenario 1. **a** Case: 1, **b** Case: 2, **c** Case: 3

(a) Case:1 **(b) Case:2** **(c) Case:3**
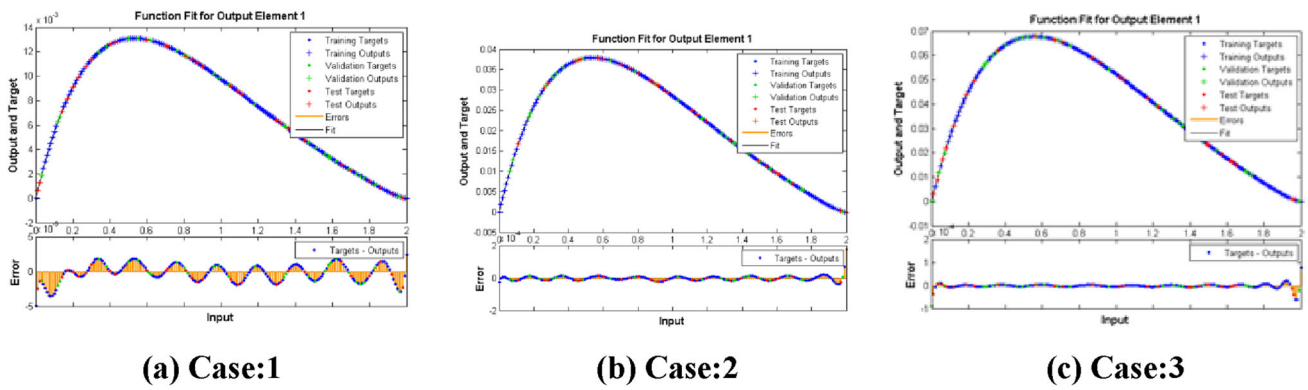
Fig. 27 Plot fit of scenario 1. **a** Case: 1, **b** Case: 2, **c** Case: 3

(a) Case:1 **(b) Case:2** **(c) Case:3**
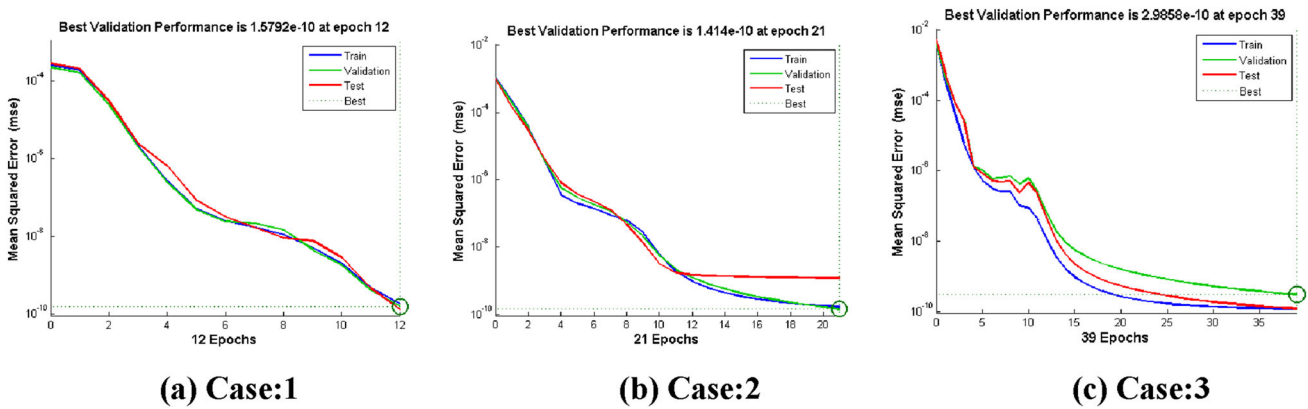
Fig. 28 Performance/convergence curves of scenario 1. **a** Case: 1, **b** Case: 2, **c** Case: 3

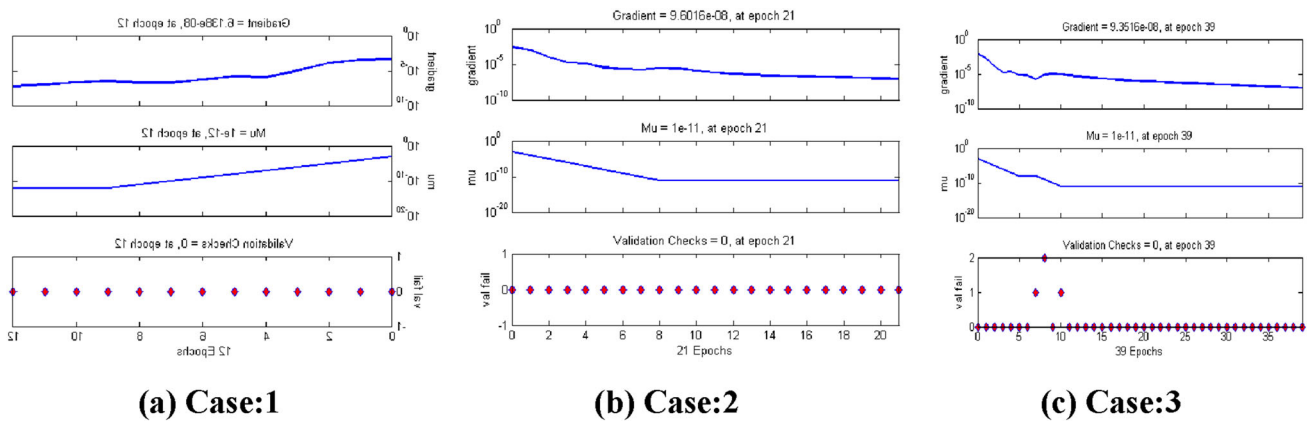**(a) Case:1** **(b) Case:2** **(c) Case:3**

Fig. 29 Training state of scenario 1. **a** Case: 1, **b** Case: 2, **c** Case: 3

the magnitude of controlling parameters, i.e., Mu and gradient, are presented in Fig. 34a–c. The value of gradient for three cases ($9.66e^{-8}$, $8.17e^{-8}$, $5.07e^{-8}$) with best fitting data sets. The magnitude of Mu for all the cases is ($1e^{-10}$, $1e^{-12}$, $1e^{-12}$). Figure 35a–c shows the best regression analysis ($R = 1$) plot for variants associated with scenario 2 with good accuracy between the target and output values.

Case study 3

The network is designed to plot the temperature profile $\theta(\eta)$ for two scenarios (γ, Pr.) for all variants associated with the Jeffrey fluid flow system and are presented graphically in Figs. 36, 37, 38, 39, 40, 41, 42, 43, 44 and 45. Figure 36a–c shows the histogram analysis of the ANN model of scenario 1 for three cases. The zero error line close to zero
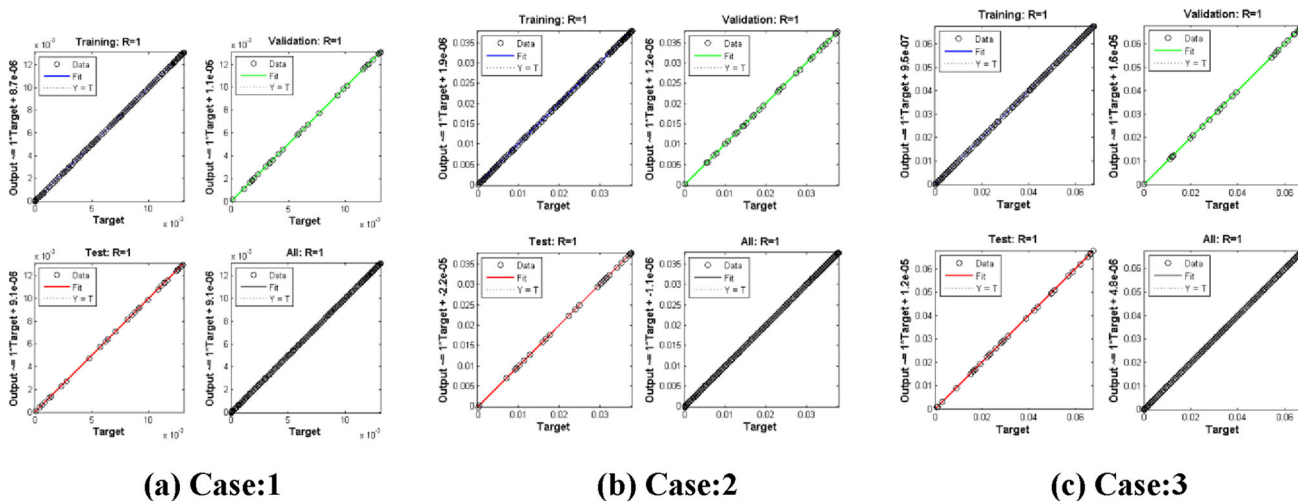
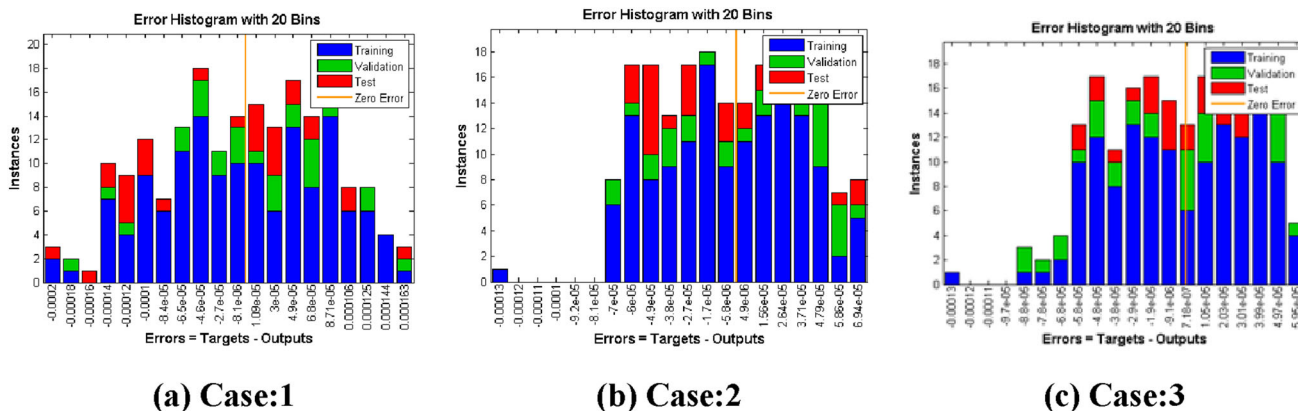**Fig. 30** Regression plot of scenario 1. **a** Case: 1, **b** Case: 2, **c** Case: 3

Fig. 31 Error histogram of scenario 2. **a** Case: 1, **b** Case: 2, **c** Case: 3
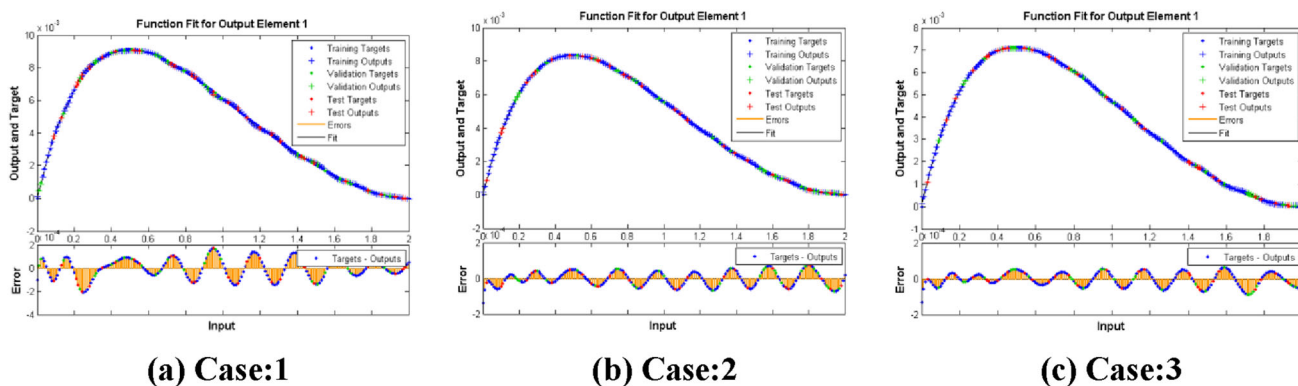
Fig. 32 Plot fit of scenario 2. **a** Case: 1, **b** Case: 2, **c** Case: 3
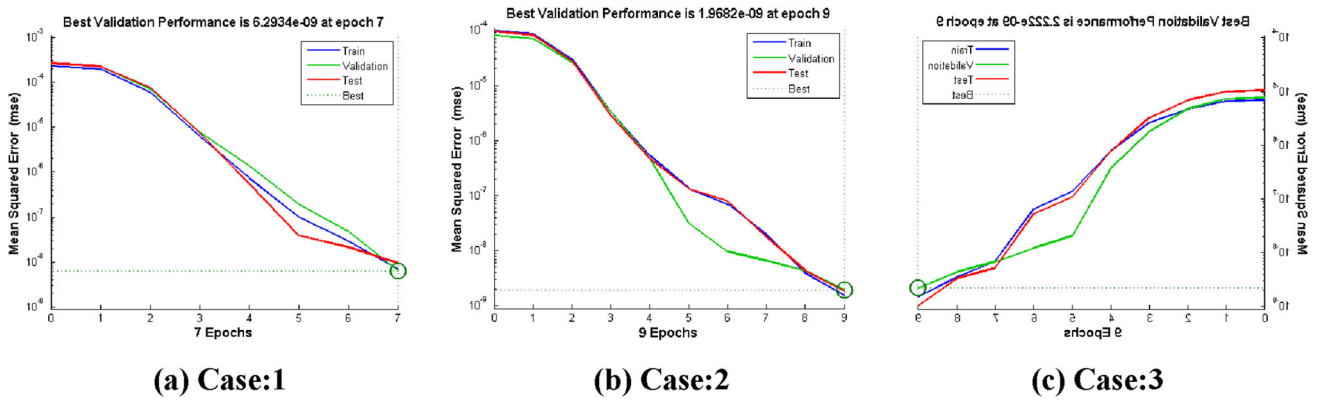
Fig. 33 Performance curve of scenario 2. **a** Case: 1, **b** Case: 2, **c** Case: 3
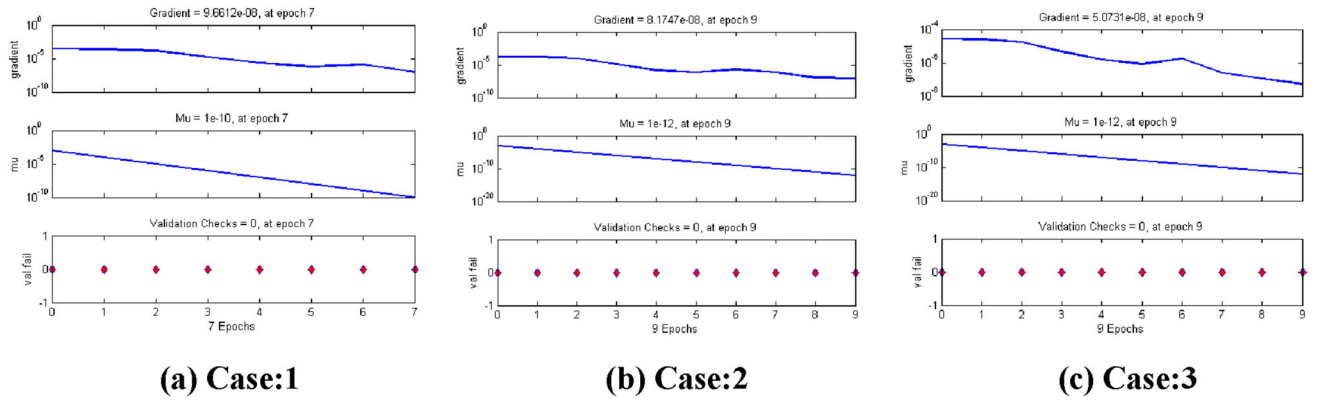
Fig. 34 Training state of scenario 2. **a** Case: 1, **b** Case: 2, **c** Case: 3
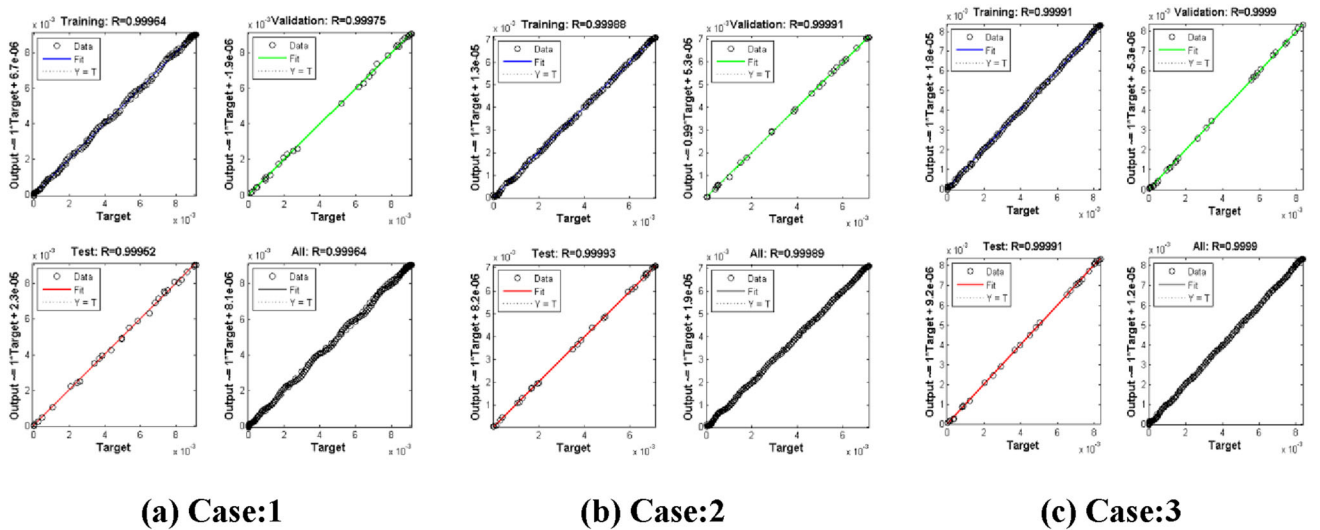
Fig. 35 Regression plot of scenario 2. **a** Case: 1, **b** Case: 2, **c** Case: 3
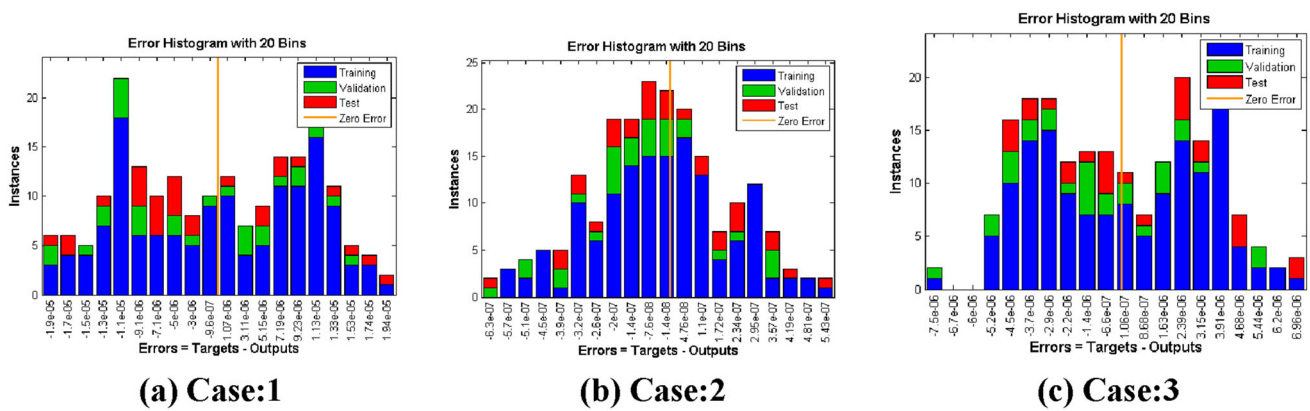
Fig. 36 Error histogram of scenario 1. **a** Case: 1. **b** Case: 2. **c** Case: 3
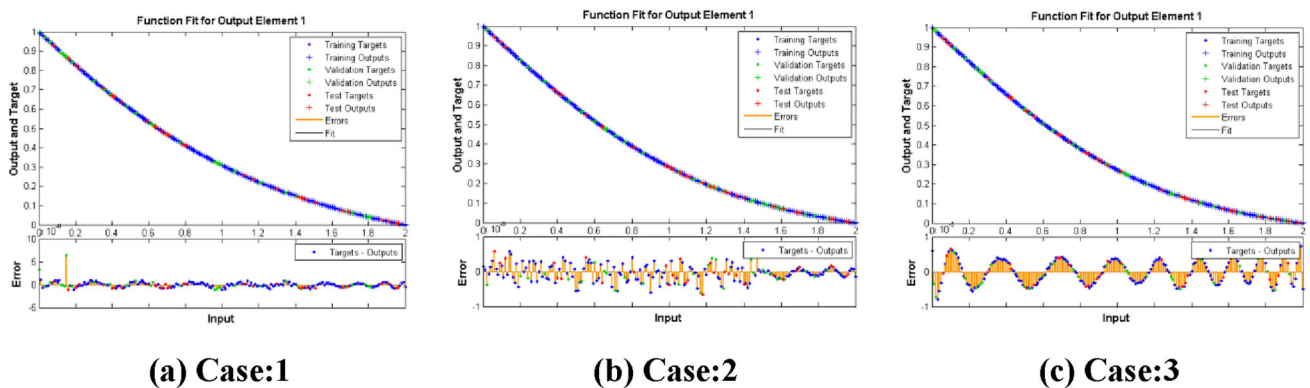
Fig. 37 Plot fit of scenario 1. **a** Case: 1. **b** Case: 2. **c** Case: 3
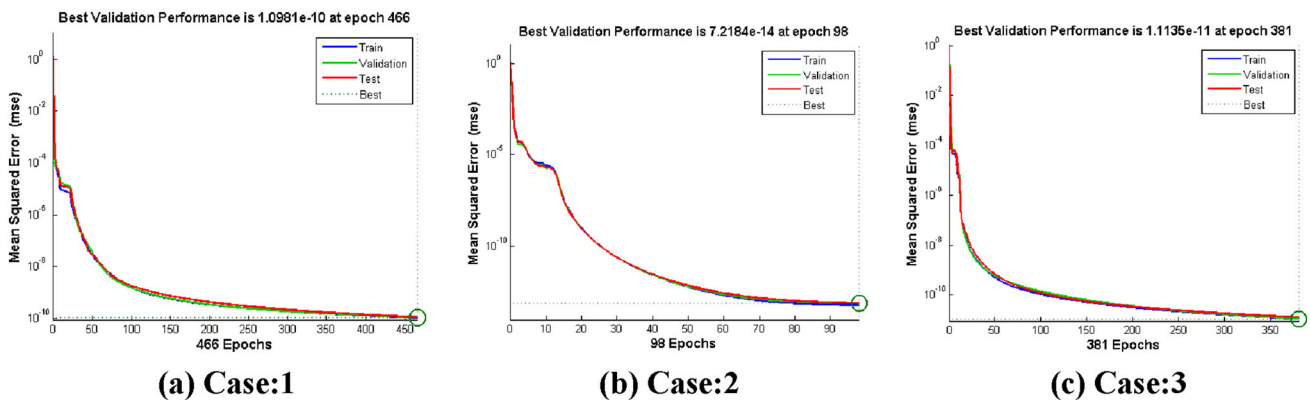

Fig. 38 Performance curve of scenario 1. **a** Case: 1. **b** Case: 2. **c** Case: 3

with negative zero error is observed in case 1, 2 and positive zero error for case 3. The error line which is close to zero represents the accuracy of data sets. Figure 37a–c demonstrates the accuracy of the data for all variants associated with scenario 1. Absolute errors values present the fitness of the network and lie in the range (-5×10^{-0} to 5×10^{-0}, -1×10^{-0} to 1×10^{-0}, -1×10^{-5} to 1×10^{-5}). Further, training of data of 3 cases of scenario 1 is illustrated in Fig. 38a–c which presents the best validation performance.

The least mean square error MSE with validation performance ($1.098096e^{-10}$, $7.21843e^{-14}$, $1.11346e^{-11}$) at the corresponding epoch (466, 98, 381) is observed. The training states of data set are presented in Fig. 39a–c. Optimized value of the weight with gradient value ($9.99e^{-8}$, $9.67e^{-8}$, $9.95e^{-8}$). The value of Mu for three cases of scenario 1 are ($1e^{-8}$, $1e^{-13}$, $1e^{-9}$) respectively. Figure 40a–c shows the best fitness analysis through regression plots with good accuracy.

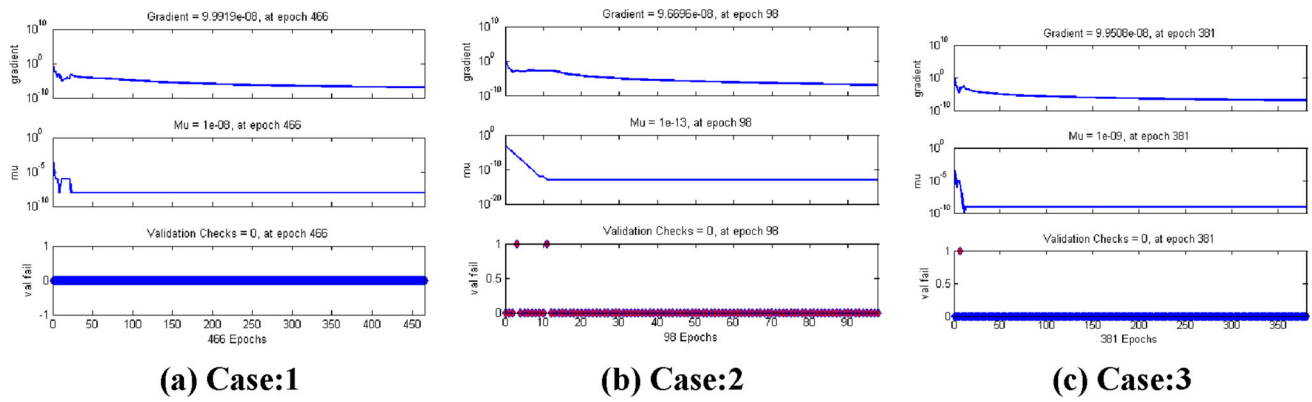**(a) Case:1** **(b) Case:2** **(c) Case:3**

Fig. 39 Training state of scenario 1. **a** Case: 1. **b** Case: 2. **c** Case: 3

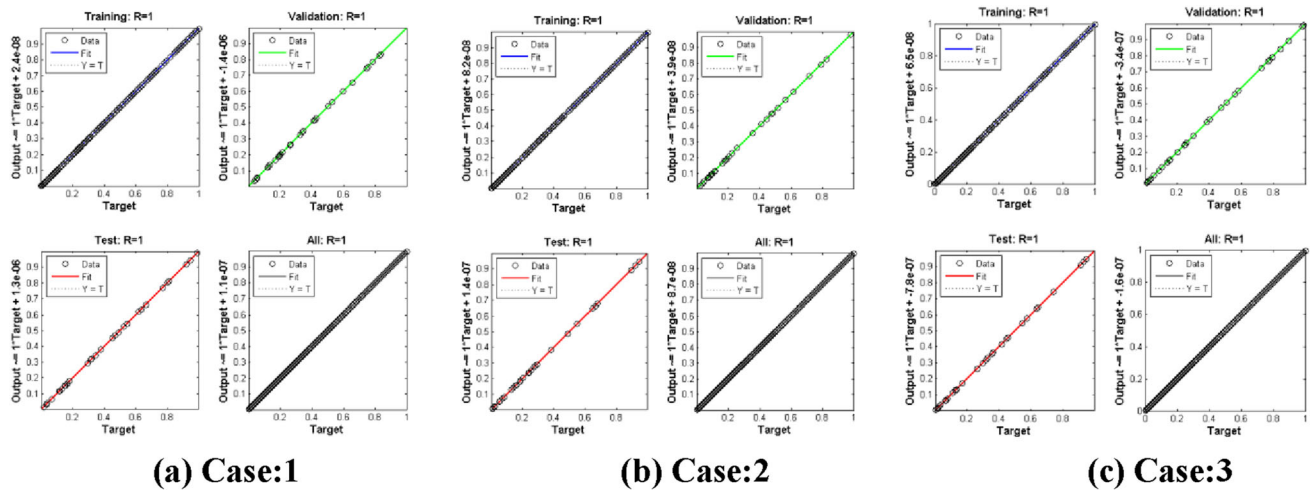**(a) Case:1** **(b) Case:2** **(c) Case:3**

Fig. 40 Regression plot of scenario 1. **a** Case: 1. **b** Case: 2. **c** Case: 3

The analysis of designed ANNs for scenario 2 of all variants is depicted in Figs. 41, 42, 43, 44 and 45. Figure 41a–c shows the plotted error histograms with negative absolute error for case 1,3 and positive absolute error for case 2. Figure 42a–c analyzed the fitting plot which shows the best error analysis and lies in the range (-5×10^{-0} to 5×10^{-0}, -5×10^{-5} to 5×10^{-5}, -1×10^{-0} to 1×10^{-0}) which authenticates the fitness of the proposed neural network. Figure 43a–c presents MSE with the best validation performances of scenario 2 for three cases. The best validation performance with minimum MSE ($1.63600e^{-12}$, $8.44640e^{-11}$, $9.51037e^{-14}$) at corresponding epoch (318, 374, 187) respectively with good validation. Figure 44a–c shows the training states of all variants of scenario 2. As it is observed from Fig. 44 training states depend upon Mu, gradient, validation checks. The value of the gradient for three cases are ($9.98e^{-8}$, $9.97e^{-8}$, $9.99e^{-8}$) at the corresponding epoch (318. 374, 187), respectively. The magnitude of Mu for three values are ($1e^{-10}$, $1e^{-8}$, $1e^{-13}$) which is close to zero with good accuracy. Figure 45 shows the best regression analysis of scenario 2 for all variants with good error fitness of ANN showing the closeness of output and target values.

Tabular description for case studies 1–3

The results presented in Tables 3, 4 and 5 describe the trials of performance of the networks for the three cases studies. Results of different scenarios of all the cases with the least value of MSE at the respective epoch are presented in tables. The value of regression (R) for all the cases are 1. Different values of Mu and gradient are presented. Time analysis are presented in tables where the maximum time for an accurate result is 6 s (see Table 6).

Concluding remarks

In the presented investigation, a Hall current effect on Magnetohydrodynamics flow with Jeffrey fluid and Heat transfer with CCHFM over a stretchable sheet with varied thickness.
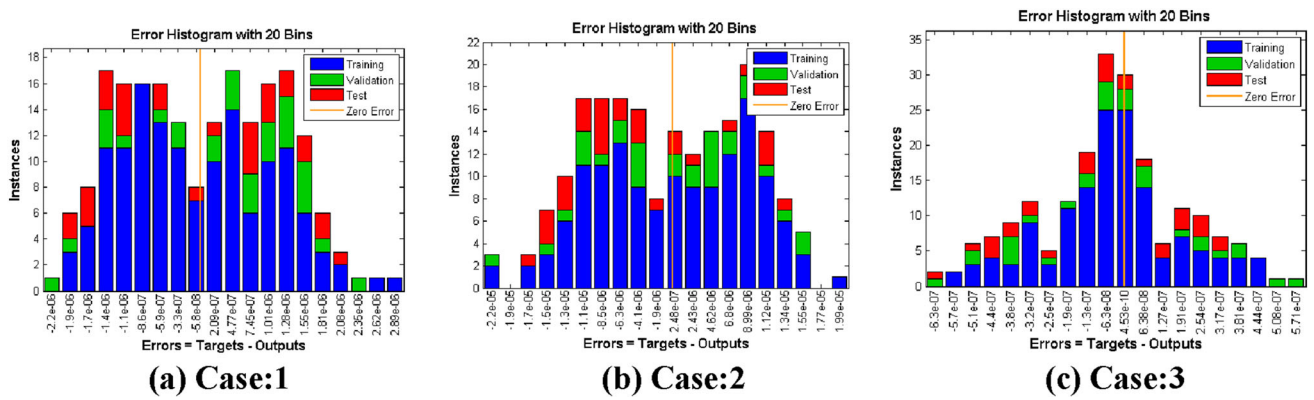
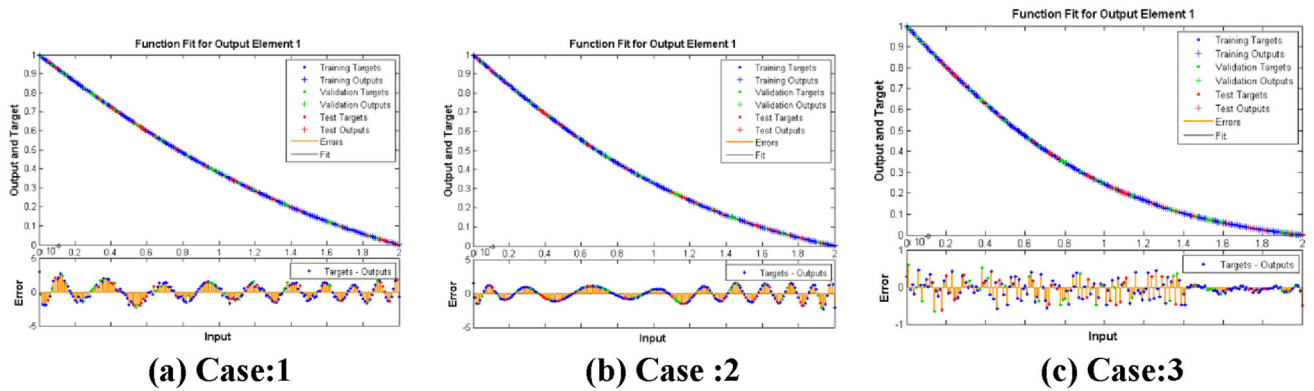**Fig. 41** Error histogram of scenario 2. **a** Case: 1. **b** Case: 2. **c** Case: 3

Fig. 42 Plot fit of scenario 2. **a** Case: 1. **b** Case: 2. **c** Case: 3
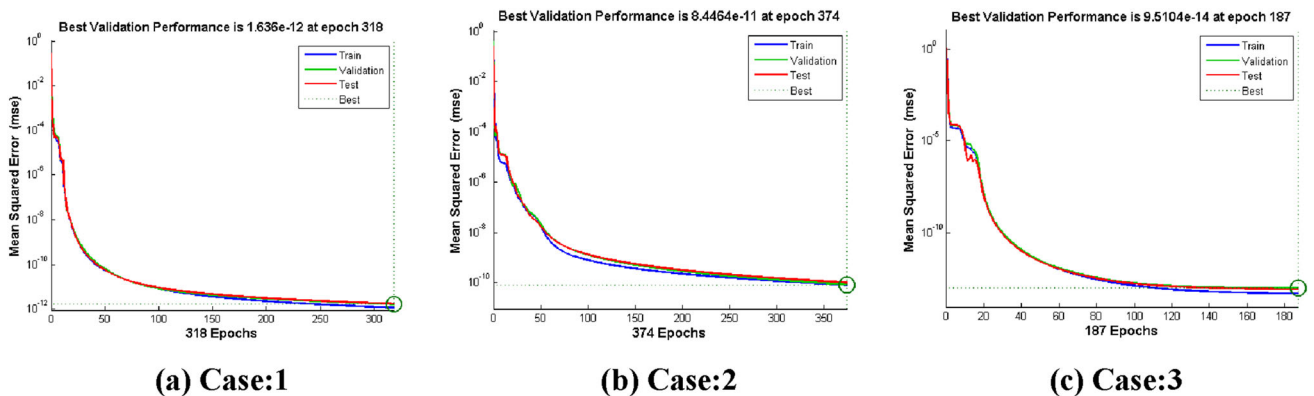
Fig. 43 Performance curve of scenario 2. **a** Case: 1. **b** Case: 2. **c** Case: 3

The results are effectively analyzed through designed ANN-LMM using error histogram, plot fit, performance, training states, regression plot. Major outcomes of the present study are summarized below:

1. Both velocity components $f'(\eta)$ and $g(\eta)$ along with the skin friction coefficient in the horizontal as well as in and z-axis direction are accelerated with the increase in Hall current parameter (m). Actually, it happens due to the controlling mechanism of electric conductivity for the fluid system, which accelerates molecular movement.

2. Magnetic field parameter reduces the thickness of momentum boundary layer along x-axis, while an increment in M will tend to reduce fluid velocity as magnetic field parameter is the ratio of electromagnetic force to the viscous force and due to this fact drag force is enhanced resulting in the increment in the skin friction coefficients along with x and z axes directions, respectively.

(a) Case:1   (b) Case:2   (c) Case:3

Fig. 44 Training state of scenario 2. **a** Case: 1. **b** Case: 2. **c** Case: 3
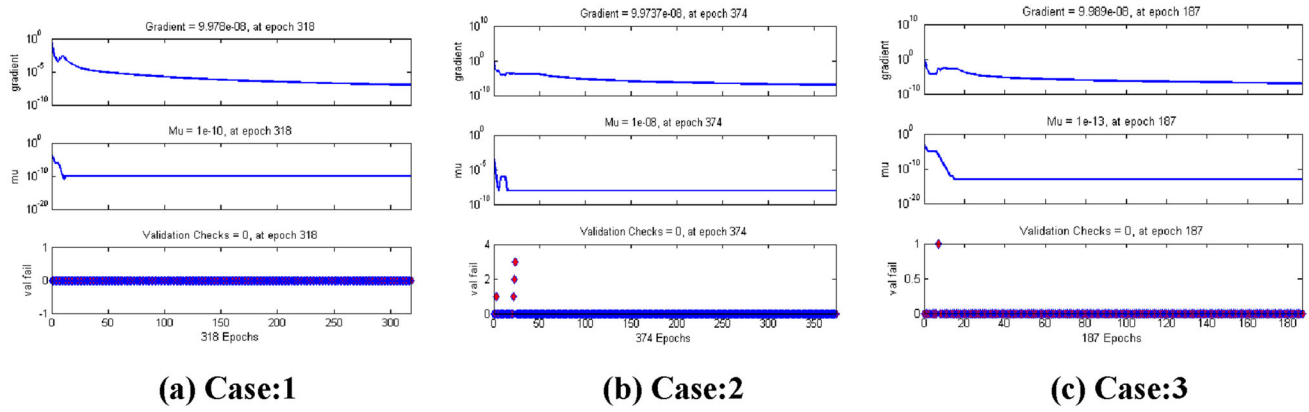

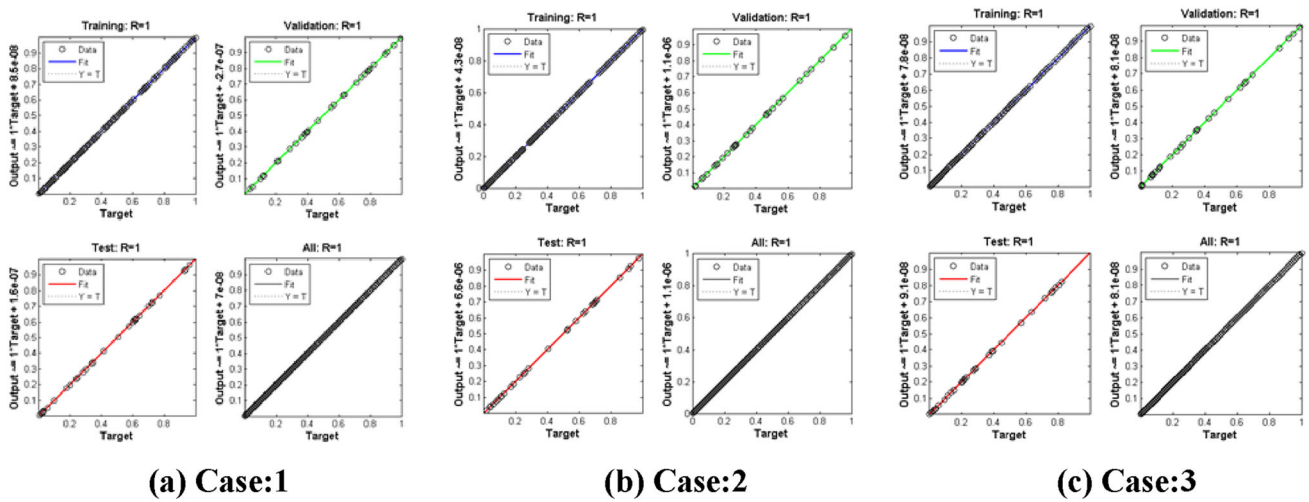(a) Case:1   (b) Case:2   (c) Case:3

Fig. 45 Regression plot of scenario 2. **a** Case: 1. **b** Case: 2. **c** Case: 3

Table 3 Convergence analysis presentation for all variants of Jeffery fluid-related CS

S	Case	Neurons	MSE-based fitness			Gradient	R	Epochs	Mu	Running time
			Training	Validation	Testing					
1	1	10	6.8527e–10	8.2625e–10	2.878e–09	9.96e–08	1	349	1.00e–08	0:00:04
	2	10	6.9184e–10	3.1567e–10	1.7468e–09	9.51e–08	1	66	1.00e–10	0:00:01
	3	10	2.2067e–09	1.5309e–09	1.6088e–09	9.99e–08	1	264	1.00e–08	0:00:04
2	1	10	4.7119e–09	1.3331e–10	5.9424e–09	1.78e–05	1	73	1.00e–08	0:00:01
	2	10	7.0416e–10	6.4100e–10	7.4295e–10	9.99e–08	1	89	1.00e–10	0:00:01
	3	10	3.1285e–10	4.3772e–10	7.6601e–10	9.798e–09	1	298	1.00e–08	0:00:03
3	1	10	5.1799e–10	1.6407e–09	5.8558e–09	9.96e–08	1	284	1.00e–09	0:00:03
	2	10	1.8271e–11	2.2375e–11	2.5498e–11	9.97e–08	1	293	1.00e–09	0:00:03
	3	10	1.0590e–09	8.8742e–10	1.8105e–09	9.83e–08	1	48	1.00e–10	0:00:02

Table 4 Convergence analysis presentation for all variants of Jeffery fluid-related CS-2

Scenario	Case	Neurons	MSE			Gradient	R	Epochs	Mu	Running time
			Training	Validation	Testing					
1	1	10	1.8441e–10	1.5791e–10	1.2956e–10	6.14e–08	1	12	1.00e–12	0:00:00
	2	10	1.6421e–10	1.4140e–10	1.1761e–09	9.60e–08	1	21	1.00e–11	0:00:00
	3	10	1.1878e–10	2.9858e–10	1.2045e–10	9.35e–08	1	39	1.00e–11	0:00:00
2	1	10	7.0042e–09	6.2933e–09	9.4006e–09	9.66e–08	1	07	1.00e–10	0:00:00
	2	10	1.5642e–09	1.9681e–09	1.8550e–09	8.17e–08	1	09	1.00e–12	0:00:00
	3	10	1.4827e–09	2.2220e–09	1.0160e–09	5.07e–08	1	09	1.00e–12	0:00:00

Table 5 Convergence analysis presentation for all variants of Jeffery fluid-related CS-3

Scenario	Case	Neurons	MSE			Gradient	R	Epochs	Mu	Running time
			Training	Validation	Testing					
1	1	10	1.0614e–10	1.0980e–10	1.2006e–10	9.99e–08	1	466	1.00e–08	0:00:06
	2	10	5.6532e–14	7.2184e–14	7.3058e–14	9.67e–08	1	98	1.00e–13	0:00:01
	3	10	1.0913e–11	1.1134e–11	1.2658e–11	9.95e–08	1	381	1.00e–09	0:00:05
2	1	10	1.1531e–12	1.6360e–12	1.7100e–12	9.98e–08	1	318	1.00e–10	0:00:04
	2	10	8.0637e–11	8.4464e–11	1.0036e–10	9.97e–08	1	347	1.00e–08	0:00:06
	3	10	4.8363e–14	9.5103e–14	8.1864e–14	9.99e–08	1	187	1.00e–13	0:00:04

Table 6 Comparison of present results with published data [45] for different values of n

n	Present results	$f''(0)$ when $\alpha = 0.25$ [45]	Present results	$f''(0)$ when $\alpha = 0.25$ [45]
– 0.6	0.8503	0.850207	– 1.4522	– 1.452134
– 0.5	– 0.0833	– 0.083289	– 1.1667	– 1.166644
– 0.33	– 0.5000	– 0.500000	– 1.0000	– 1.0000000
0.0	– 0.7843	– 0.784284	– 0.9576	– 0.957648
0.5	– 0.9338	– 0.933828	– 0.9799	– 0.979948
3.0	– 1.0905	– 1.090490	– 1.0359	– 1.035867
5.0	– 1.1186	– 1.118587	– 1.0486	– 1.048610
7.0	– 1.1323	– 1.132388	– 1.0550	– 1.055043
10.0	– 1.1433	– 1.143316	– 1.0603	– 1.060323

Whereas along x-axis and z-axis the skin friction coefficient increases for M.

3. The temperature profile for $\theta(\eta)$ shows a reduction with an increment of Pr as is the ratio of momentum diffusivity to the thermal diffusivity as due to the large value of Pr, the thermal diffusivity becomes low which declines the temperature profile.

4. The velocity component $f'(\eta)$ tends to increase with an increment in Deborah number β, while the opposite behavior is found for $g(\eta)$.

5. Velocity profile $f'(\eta)$ decreases for larger value of ratios of relaxation to the retardation time (λ_1) while $g(\eta)$ shows opposite behavior.

6. With an increment in relaxation time of the heat flux γ tend to decrease temperature profile $\theta(\eta)$.

7. Local Nusselt number Nu_x increase with increment in the Pr, α, m, β and decreases with increase in M, λ_1, γ/As the larger value of the Nu_x corresponds to more effective convection in the fluid flow system.

8. In the Artificial neural network, the error between the target and output value after training are analyzed by an error histogram. The Regression (R) of the trained data set for all the cases is 1.i-e ($R = 1$).

In the future, one may exploit/investigate the strength of the proposed ANN-LMM in various applications arising

in the studies of nanofluids [46–52] and nonlinear systems [53–55].

Declarations

Conflict of interest The authors declared that they have no conflict of interest.

References:

1. Shah Z, Alzahrani EO, Alghamdi W, Ullah MZ (2020) Influences of electrical MHD and Hall current on squeezing nanofluid flow inside rotating porous plates with viscous and joule dissipation effects. J Therm Anal Calorim 140(3):1215–1227

2. Kumar D, Singh AK, Kumar D (2020) Influence of heat source/sink on MHD flow between vertical alternate conducting walls with Hall effect. Phys A 544:123562

3. Opanuga AA, Adesanya SO, Okagbue HI, Agboola OO (2020) Impact of Hall current on the entropy generation of radiative MHD mixed convection casson fluid. Int J Appl Comput Math 6(2):1–18

4. Akbar Y, Abbasi FM, Shehzad SA (2020) Effectiveness of Hall current and ion slip on hydromagnetic biologically inspired flow of Cu$-$Fe$_3$O$_4$/H$_2$O hybrid nanomaterial. Phys Scr 96(2):025210

5. Awan SE, Raja MAZ, Gul F, Khan ZA, Mehmood A, Shoaib M (2021) Numerical Computing Paradigm for Investigation of Micropolar Nanofluid Flow Between Parallel Plates System with Impact of Electrical MHD and Hall Current. Arab J Sci Eng 46(1):645–662

6. Shah Z, Islam S, Gul T, Bonyah E, Khan MA (2018) The electrical MHD and hall current impact on micropolar nanofluid flow between rotating parallel plates. Results Phys 9:1201–1214

7. Chu YM, Nazeer M, Khan MI, Hussain F, Rafi H, Qayyum S, Abdelmalek Z (2020) Combined impacts of heat source/sink, radiative heat flux, temperature dependent thermal conductivity on forced convective Rabinowitsch fluid. Int Commun Heat Mass Transf 120:105011.

8. Hayat T, Riaz R, Aziz A, Alsaedi A (2020) Influence of Arrhenius activation energy in MHD flow of third grade nanofluid over a nonlinear stretching surface with convective heat and mass conditions. Phys A Stat Mech Appl 549:124006

9. Riaz A, Zeeshan A, Bhatti MM, Ellahi R (2020) Peristaltic propulsion of Jeffrey nano-liquid and heat transfer through a symmetrical duct with moving walls in a porous medium. Phys A 545:123788

10. Sreelakshmi K, Sarojamma G, Murthy JV (2018) Homotopy analysis of an unsteady flow heat transfer of a Jeffrey nanofluid over a radially stretching convective surface. J Nanofluids 7(1):62–71

11. Khan MWA, Khan MI, Hayat T, Alsaedi A (2020) Numerical solution of MHD flow of power law fluid subject to convective boundary conditions and entropy generation. Comput Methods Programs Biomed 188:105262

12. Noreen S, Riaz A, Lu D (2020) Soret-Dufour effects in electroosmotic biorheological flow of Jeffrey fluid. Heat Transfer 49(4):2355–2374

13. Shahzad F, Sagheer M, Hussain S (2018) Numerical simulation of magnetohydrodynamic Jeffrey nanofluid flow and heat transfer over a stretching sheet considering Joule heating and viscous dissipation. AIP Adv 8(6):065316

14. Patel N, Meher R (2018) Analytical investigation of Jeffery-Hemal flow with magnetic field by differential transform method. Int J Adv Appl Math Mech 6:1–9

15. Vaidya H, Rajashekhar C, Divya BB, Manjunatha G, Prasad KV, Animasaun IL (2020) Influence of transport properties on the peristaltic MHD Jeffrey fluid flow through a porous asymmetric tapered channel. Results Phys 18:103295

16. Nazeer M, Hussain F, Ahmad MO, Saeed S, Khan MI, Kadry S, Chu YM (2021) Multi-phase flow of Jeffrey Fluid bounded within magnetized horizontal surface. Surf Interfaces 22:100846

17. Waqas M (2021) Diffusion of stratification based chemically reactive Jeffrey liquid featuring mixed convection. Surf Interfaces 23:100783

18. Malik HT, Farooq M, Ahmad S (2020) Significance of nonlinear stratification in convective Falkner-Skan flow of Jeffrey fluid near the stagnation point. Int Commun Heat Mass Transf 120:105032

19. Ahmed F (2021) Fully developed forced convective Jeffrey fluid flow through concentric pipes annular duct. Eur Physi J Plus 136(1):1–20

20. Ali A, Saleem S, Mumraiz S, Saleem A, Awais M, Khan Marwat DN (2020) Investigation on TiO$_2$–Cu/H$_2$O hybrid nanofluid with slip conditions in MHD peristaltic flow of Jeffrey material. J Therm Anal Calorim 143:1–12

21. Asha SK, Sunitha G (2020) Thermal radiation and Hall effects on peristaltic blood flow with double diffusion in the presence of nanoparticles. Case Stud Therm Eng 17:100560

22. Sinha VK, Kumar B, Seth GS, Nandkeolyar R (2020) Features of Jeffrey fluid flow with Hall current: a spectral simulation. Pramana J Phys 94(1):1–8

23. Abeykoon C (2020) Compact heat exchangers–Design and optimization with CFD. Int J Heat Mass Transf 146:118766

24. Cattaneo C (1948) Sulla conduzione del calore. In: Atti Semin Mat Fis Univ Modena Reggio Emilia, Universitia di Modena, pp 83–101

25. Christov CI (2009) On frame indifferent formulation of the Maxwell-Cattaneo model of finite-speed heat conduction. Mech Res Commun 36:481–486

26. Ciarletta M, Straughan B (2010) Uniqueness and structural stability for the Cattaneo—Christov equations. Mech Res Commun 37:445–447

27. Tassaddiq A (2021) Impact of Cattaneo–Christov heat flux model on MHD hybrid nano-micropolar fluid flow and heat transfer with viscous and joule dissipation effects. Sci Rep 11(1):1–14

28. Awais M, Awan SE, Iqbal K, Khan ZA, Raja MAZ (2018) Hydromagnetic mixed convective flow over a wall with variable thickness and Cattaneo–Christov heat flux model: OHAM analysis. Results Phys 8:621–627

29. Hayat T, Khan SA, Khan MI, Momani S, Alsaedi A (2020) Cattaneo–Christov (CC) heat flux model for nanomaterial stagnation point flow of Oldroyd-B fluid. Comput Methods Programs Biomed 187:105247

30. Alamri S, Khan AA, Azeez M (2019) Effects of mass transfer on MHD fluid towards stretching cylinder: a novel perspective of Cattaneo–Christov heat flux model. Phys Lett A 383:276–281

31. Shah Z, Alzahrani EO, Dawar A, Ullah A, Khan I (2020) Influence of Cattaneo–Christov model on Darcy-Forchheimer flow of Micropolar Ferrofluid over a stretching/shrinking sheet. Int Commun Heat Mass Transfer 110:104385

32. Ahmad S, Nadeem S (2020) Flow analysis by Cattaneo–Christov heat flux in the presence of Thomson and Troian slip condition. Appl Nanosci 10:1–15

33. Khan M, Ahmed A, Irfan M, Ahmed J (2020) Analysis of Cattaneo–Christov theory for unsteady flow of Maxwell fluid over stretching cylinder. J Therm Anal Calorim 144:1–10

34. Robbins H, Monro S (1951) A stochastic approximation method. Ann Math Stat 22:400–407

35. Mehmood A, Afsar K, Zameer A, Awan SE, Raja MAZ (2019) Integrated intelligent computing paradigm for the dynamics of micropolar fluid flow with heat transfer in a permeable walled channel. Appl Soft Comput 79:139–162

36. Sheikholeslami M, Gerdroodbary MB, Moradi R, Shafee A, Li Z (2019) Application of Neural Network for estimation of heat transfer treatment of Al2O3-H2O nanofluid through a channel. Comput Methods Appl Mech Eng 344:1–12

37. Awan SE, Raja MAZ, Awais M, Shu CM (2021) Intelligent Bayesian regularization networks for bio-convective nanofluid flow model involving gyro-tactic organisms with viscous dissipation, stratification and heat immersion. Eng Appl Comput Fluid Mech 15(1):1508–1530

38. Awais M, Bibi M, Raja MAZ, Awan SE, Malik MY (2021) Intelligent numerical computing paradigm for heat transfer effects in a Bodewadt flow. Surf Interfaces 26:101321

39. Raja MAZ, Awan SE, Shoaib M, Awais M (2022) Backpropagated intelligent networks for the entropy generation and joule heating in hydromagnetic nanomaterial rheology over surface with variable thickness. Arab J Sci Eng, pp 1–25

40. Qureshi IH, Awais M, Awan SE, Abrar MN, Raja MAZ, Alharbi SO, Khan I (2021) Influence of radially magnetic field properties in a peristaltic flow with internal heat generation: numerical treatment. Case Stud Therm Eng 26:101019

41. Awan SE, Awais M, Raja MAZ, Parveen N, Ali HM, Khan WU, He Y (2021) Numerical treatment for dynamics of second law analysis and magnetic induction effects on ciliary induced peristaltic transport of hybrid nanomaterial. Front Phys 9:68

42. Awan SE, Raja MAZ, Mehmood A, Niazi SA, Siddiqa S (2020) Numerical treatments to analyze the nonlinear radiative heat transfer in MHD nanofluid flow with solar energy. Arab J Sci Eng 45:4975–4994

43. Awais M, Awan SE, Raja MAZ, Parveen N, Khan WU, Malik MY, He Y (2021) Effects of variable transport properties on heat and mass transfer in MHD bioconvective nanofluid rheology with gyrotactic microorganisms: numerical approach. Coatings 11(2):231

44. Hayat T, Khan MI, Farooq M, Alsaedi A, Waqas M, Yasmeen T (2016) Impact of Cattaneo–Christov heat flux model in flow of variable thermal conductivity fluid over a variable thicked surface. Int J Heat Mass Transf 99:702–710

45. Fang T, Zhang J, Zhong Y (2012) Boundary layer flow over a stretching sheet with variable thickness. Appl Math Comput 218(13):7241–7252

46. Parveen N, Awais M, Awan SE, Shah SA, Yuan A, Nawaz M, Akhtar R, Malik MY (2021) Thermophysical properties of chemotactic microorganisms in bio-convective peristaltic rheology of nano-liquid with slippage, Joule heating and viscous dissipation. Case Stud Therm Eng 27:101285

47. Shi QH, Ahmed B, Ahmad S, Khan SU, Sultan K, Bashir MN, Khan MI, Shah NA, Chung JD (2021) Dual solution framework for mixed convection flow of Maxwell nanofluid instigated by exponentially shrinking surface with thermal radiation. Sci Rep 11(1):1–12

48. Awais M, Raja MAZ, Awan SE, Shoaib M, Ali HM (2021) Heat and mass transfer phenomenon for the dynamics of Casson fluid through porous medium over shrinking wall subject to Lorentz force and heat source/sink. Alex Eng J 60(1):1355–1363

49. Li YX, Mishra SR, Pattnaik PK, Baag S, Li YM, Khan MI, Khan NB, Alaoui MK, Khan SU (2021) Numerical treatment of time dependent magnetohydrodynamic nanofluid flow of mass and heat transport subject to chemical reaction and heat source. Alex Eng J 61:2484–2491

50. Awais M, Awan SE, Raja MAZ, Shoaib M (2021) Effects of Gyro-Tactic organisms in bio-convective nano-material with heat immersion, stratification, and viscous dissipation. Arab J Sci Eng 46(6):5907–5920

51. Siddiqa S, Naqvi SB, Begum N, Awan SE, Hossain MA (2018) Thermal radiation therapy of biomagnetic fluid flow in the presence of localized magnetic field. Int J Therm Sci 132:457–465

52. Awan SE, Raja MAZ, Awais M, Bukhari SHR (2022) Backpropagated intelligent computing networks for 3D nanofluid rheology with generalized heat flux. Waves in Random Complex Media, pp 1–31 (in press). https://doi.org/10.1080/17455030.2022.2039417

53. Shoaib M, Raja MAZ, Khan MAR, Farhat I, Awan SE (2021) Neuro-computing networks for entropy generation under the influence of MHD and thermal radiation. Surf Interfaces 25:101243

54. Jin J (2021) A robust zeroing neural network for solving dynamic nonlinear equations and its application to kinematic control of mobile manipulator. Complex Intell Syst 7(1):87–99

55. Raja MAZ, Sabati M, Parveen N, Awais M, Awan SE, Chaudhary NI, Shoaib M, Alquhayz H (2021) Integrated intelligent computing application for effectiveness of Au nanoparticles coated over MWCNTs with velocity slip in curved channel peristaltic flow. Sci Rep 11(1):1–20